



# First Identification of 10 kpc [C II] 158 $\mu$ m Halos around Star-forming Galaxies at $z = 5-7$

Seiji Fujimoto<sup>1,2,3</sup> , Masami Ouchi<sup>1,4</sup> , Andrea Ferrara<sup>4,5</sup> , Andrea Pallottini<sup>5,6</sup>, R. J. Ivison<sup>7,8</sup> , Christoph Behrens<sup>5</sup>, Simona Gallerani<sup>5</sup>, Shohei Arata<sup>9</sup>, Hidenobu Yajima<sup>10</sup>, and Kentaro Nagamine<sup>4,9,11</sup>

<sup>1</sup> Institute for Cosmic Ray Research, The University of Tokyo, Kashiwa, Chiba 277-8582, Japan; [sfseiji@icrr.u-tokyo.ac.jp](mailto:sfseiji@icrr.u-tokyo.ac.jp)

<sup>2</sup> National Astronomical Observatory of Japan, 2-21-1, Osawa, Mitaka, Tokyo, Japan

<sup>3</sup> Research Institute for Science and Engineering, Waseda University, 3-4-1 Okubo, Shinjuku, Tokyo 169-8555, Japan

<sup>4</sup> Kavli Institute for the Physics and Mathematics of the Universe (WPI), University of Tokyo, Kashiwa 277-8583, Japan

<sup>5</sup> Scuola Normale Superiore, Piazza dei Cavalieri 7, I-56126 Pisa, Italy

<sup>6</sup> Centro Fermi, Museo Storico della Fisica e Centro Studi e Ricerche “Enrico Fermi” Piazza del Viminale 1, Roma, I-00184, Italy

<sup>7</sup> European Southern Observatory, Karl Schwarzschild Str. 2, D-85748 Garching, Germany

<sup>8</sup> Institute for Astronomy, University of Edinburgh, Royal Observatory Blackford Hill, Edinburgh EH9 3HJ, UK

<sup>9</sup> Theoretical Astrophysics, Department of Earth and Space Science, Graduate School of Science, Osaka University, Toyonaka, Osaka 560-0043, Japan

<sup>10</sup> Center of Computational Sciences University of Tsukuba, Ibaraki 305-8577, Japan

<sup>11</sup> Department of Physics & Astronomy, University of Nevada, Las Vegas, 4505 S. Maryland Parkway, Las Vegas, NV 89154-4002, USA

Received 2019 February 10; revised 2019 September 19; accepted 2019 September 24; published 2019 December 16

## Abstract

We report the discovery of 10 kpc [C II] 158  $\mu$ m halos surrounding star-forming galaxies in the early universe. We choose deep Atacama Large Millimeter/submillimeter Array data for 18 galaxies, each with a star formation rate of  $\simeq 10-70 M_{\odot}$  with no signature of an active galactic nucleus whose [C II] lines are individually detected at  $z = 5.153-7.142$ , and we conduct stacking of the [C II] lines and dust continuum in the  $uv$ -visibility plane. The radial profiles of the surface brightnesses show a 10 kpc scale [C II] halo at the  $9.2\sigma$  level, significantly more extended than the *Hubble Space Telescope* stellar continuum data by a factor of  $\sim 5$  on the exponential-profile basis, as well as the dust continuum. We compare the radial profiles of [C II] and Ly $\alpha$  halos universally found in star-forming galaxies at this epoch, and we find that the scale lengths agree within the  $1\sigma$  level. While two independent hydrodynamic zoom-in simulations match the dust and stellar continuum properties, the simulations cannot reproduce the extended [C II] line emission. The existence of the extended [C II] halo is evidence of outflow remnants in the early galaxies and suggests that the outflows may be dominated by cold-mode outflows expelling the neutral gas.

**Key words:** galaxies: evolution – galaxies: formation – galaxies: high-redshift

## 1. Introduction

Galaxy size and morphological studies in the early universe provide important insights into the initial stage of galaxy formation and evolution. The size and morphology in the rest-frame ultraviolet (UV) and far-infrared (FIR) wavelengths trace the areas of young star formation and the active starbursts that are less and heavily obscured by dust, respectively. The [C II]  $^2P_{3/2} \rightarrow ^2P_{1/2}$  fine-structure transition at 1900.5469 GHz (157.74  $\mu$ m) is a dominant coolant of the interstellar medium (ISM) in galaxies (e.g., Stacey et al. 1991; De Looze et al. 2014), whose size and morphology are strong probes of ISM properties. Comparing the size and morphology in the rest-frame UV+FIR continuum and the [C II] 158  $\mu$ m line is thus important to comprehensively understand the evolutionary process via star formation surrounded by the ISM.

The *Hubble Space Telescope* (*HST*) has revealed the size and morphological properties in the rest-frame UV wavelengths for high-redshift galaxies up to  $z \sim 10$  (e.g., Oesch et al. 2010; Ono et al. 2013; Shibuya et al. 2015; Bouwens et al. 2017; Kawamata et al. 2018). These *HST* studies show that star-forming galaxies generally have an exponential-disk profile and become compact toward high redshifts.

The Atacama Large Millimeter/submillimeter Array (ALMA) has opened our views to obscured star formation and the [C II] line properties in the rest-frame FIR wavelengths up to  $z \sim 7$  (e.g., Capak et al. 2015; Maiolino et al. 2015; Watson et al. 2015; Knudsen et al. 2016; Pentericci et al. 2016; Matthee et al. 2017; Carniani et al. 2018; Hashimoto et al. 2019; Smit et al. 2018). There have also been several attempts to measure the size and

morphology in the rest-frame FIR continuum and the [C II] line for such high-redshift galaxies at  $z \sim 5-7$ , where Carniani et al. (2018) report that the effective radius of the [C II] line emitting region is larger than that of the rest-frame UV region. However, large uncertainties still remain due to the small number statistics and observational challenges.

One critical challenge is sensitivity. The recent ALMA studies show that a signal-to-noise ratio (S/N)  $> 10$  is needed to obtain reliable size measurement results on both the image-based and visibility-based analyses (e.g., Simpson et al. 2015; Ikarashi et al. 2015), while the majority of the previous ALMA detections of the dust continuum and the [C II] line from  $z \sim 5-7$  galaxies show an S/N less than 10. If the S/N level is poor, noise fluctuations significantly affect the profile fitting results. Moreover, Hodge et al. (2016) show that the combination of the original smoothed galaxy profile and the noise fluctuations can make the morphology more clumpy. To obtain reliable size and morphological results, extensively deep observations are thus required.

In this paper, we determine the size and morphology for the dust continuum and the [C II] line in the star-forming galaxies at  $z = 5-7$  via the stacking technique in the  $uv$ -visibility plane, utilizing new and archival deep ALMA Band 6/7 data. In conjunction with deep *HST* images, we study the general morphology of the total star formation and the ISM in the epoch of reionization. The structure of this paper is as follows. In Section 2, the observations and the data reduction are described. Section 3 outlines the method of [C II] line detections, line velocity width, source position measurements,

**Table 1**  
Our ALMA Sample

Target	R.A. (J2000)	Decl. (J2000)	$z_{[\text{C II}]}$ ( $z_{\text{Ly}\alpha}$ )	$M_{\text{UV}}$ (mag)	$\text{EW}_{\text{Ly}\alpha}$ (Å)	$\sigma_{\text{cont.}}^a$ ( $\mu\text{Jy}/\text{beam}$ )	Beam ( $'' \times ''$ )	ALMA ID	<i>HST</i>	Reference
			(1)	(2)	(3)	(4)	(5)	(6)	(7)	(8)
Literature										
WMH5	36.612542	−4.877333	6.069 (6.076)	−22.6	13.0	8	$0.50 \times 0.46$	2013.1.00815.S 2015.1.00834.S	N	W15, J17 W15, J17
CLM1	37.012319	−4.271706	6.166 (6.176)	−22.6	50.0	18	$0.52 \times 0.45$	2013.1.00815.S	N	W15
COS301855	150.125803	2.266613	6.854 (···)	−21.9	−2.9	27	$1.08 \times 0.74$	2015.1.01111.S	Y	S18 (S15)
COS298703	150.124400	2.217294	6.808 (6.816)	−22.0	16.2	25	$1.07 \times 0.74$	2015.1.01111.S	Y	S18 (S15)
NTTDF6345	181.403878	−7.756192	6.698 (6.701)	−21.5	15.0	20	$1.25 \times 0.97$	2015.1.01105.S	N	P16
BDF2203	336.958267	−35.147529	6.122 (6.118)	−20.9	9.9	20	$1.85 \times 1.05$	2016.1.01240.S	N <sup>b</sup>	C18
COS13679	150.099014	2.343517	7.142 (7.145)	−21.4	15.0	18	$0.85 \times 0.85$	2015.1.01105.S	N <sup>c</sup>	P16
COS24108	150.197356	2.478931	6.623 (6.629)	−21.6	27.0	20	$0.81 \times 0.75$	2015.1.01105.S	N <sup>c</sup>	P16
H <sub>z</sub> 1	149.971828	2.118142	5.689 (5.690)	−22.0	5.3	27	$0.75 \times 0.52$	2012.1.00523.S	Y	C15 (B17)
H <sub>z</sub> 2	150.517186	1.928936	5.670 (5.670)	−21.9	6.9	35	$0.83 \times 0.53$	2012.1.00523.S	N <sup>c</sup>	C15 (B17)
H <sub>z</sub> 3	150.039247	2.3371611	5.542 (5.546)	−21.7	−3.6	47	$0.77 \times 0.42$	2012.1.00523.S	Y	C15 (B17)
H <sub>z</sub> 4	149.618760	2.051850	5.544 (5.310)	−22.3	10.2	64	$0.89 \times 0.51$	2012.1.00523.S	Y	C15 (B17)
H <sub>z</sub> 6	150.089576	2.586324	5.293 (5.290)	−22.8	8.0	32	$0.67 \times 0.50$	2012.1.00523.S	Y	C15 (B17)
H <sub>z</sub> 7	149.876925	2.134061	5.253 (5.250)	−21.8	9.8	35	$0.47 \times 0.38$	2012.1.00523.S	Y	C15 (B17)
H <sub>z</sub> 8	150.016894	2.626631	5.153 (5.148)	−21.8	27.1	30	$0.40 \times 0.29$	2012.1.00523.S	Y	C15 (B17)
H <sub>z</sub> 9	149.965404	2.378358	5.541 (5.548)	−21.9	14.4	43	$0.64 \times 0.54$	2012.1.00523.S	Y	C15 (B17)
New Detection										
NB816-S-61269	34.438567	−5.493392	5.684 (5.688)	−20.4	93.3	22	$0.45 \times 0.42$	2012.1.00602.S	N	F16
WMH13	149.985580	2.207528	5.985 (5.983)	−22.0	27.0	16	$1.15 \times 0.89$	2013.1.00815.S	N	W15

**Notes.** (1) Spectroscopic redshift determined by the [C II] (Ly $\alpha$ ) line emission. (2) Absolute magnitudes. (3) Rest-frame Ly $\alpha$  EW. (4)  $1\sigma$  noise measured by the standard deviation of the pixel values in the continuum map before primary beam correction. (5) Synthesized beam size of our ALMA maps (weighting = “natural”). (6) ALMA project ID. (7) “Y” (“N”) indicates the sources (not) included in the ALMA-*HST* sample. (8) ALMA (*HST*) data reference (W15: Willott et al. 2015, J17: Jones et al. 2017, S18: Smit et al. 2018, P16: Pentericci et al. 2016, C18: Carniani et al. 2018, S15: Smit et al. 2015, C15: Capak et al. 2015, B17: Barisic et al. 2017, F16: Fujimoto et al. 2016).

<sup>a</sup> Our additional flagging and difference in the imaging parameter setting may produce different values from the data references.

<sup>b</sup> Although there is the F105W data, we do not include this source in the ALMA-*HST* sample because of the differences in the point-spread function and the rest-frame wavelength from the F160W data.

<sup>c</sup> Although there is the F160W data, we do not include these sources in the ALMA-*HST* sample because of the large offsets even after the astrometry correction (see text).

and the stacking processes of ALMA and *HST* data. We report the results for the radial profiles of the [C II] line, rest-frame FIR, and rest-frame UV wavelengths in Section 4. In Section 5, we discuss the physical origin of the extended [C II] line emission, comparing with the zoom-in cosmological simulation results. A summary of this study is presented in Section 6.

Throughout this paper, we assume a flat universe with  $\Omega_m = 0.3$ ,  $\Omega_\Lambda = 0.7$ ,  $\sigma_8 = 0.8$ , and  $H_0 = 70 \text{ km s}^{-1} \text{ Mpc}^{-1}$ . We use magnitudes in the AB system (Oke & Gunn 1983).

## 2. Sample and Data Reduction

### 2.1. Our ALMA Sample

The sample is drawn mainly from the literature (Capak et al. 2015; Willott et al. 2015; Pentericci et al. 2016; Jones et al. 2017; Carniani et al. 2018; Smit et al. 2018), selecting only star-forming galaxies at  $z > 5$  whose [C II] lines have been detected (at  $S/N \gtrsim 5$ ) with ALMA. To obtain reliable results for representative galaxies in the early universe, we limit our sample to galaxies with (i) star formation rates (SFRs)  $< 100 M_\odot \text{ yr}^{-1}$ ; (ii) no indication of active galactic nucleus (AGN) activity; (iii) no giant Ly $\alpha$  systems, such as Himiko (Ouchi et al. 2009) and CR7 (Matthee et al. 2015); (iv) no signs of gravitational lensing, that is, galaxies behind massive galaxy clusters; (v) [C II] line emission with an FWHM broader than  $80 \text{ km s}^{-1}$ ; and (vi) [C II] line detections that

are reproduced in our own data reduction. We adopt (v) because the thermal noise fluctuation can produce peaky, false source signals even with  $S/N > 5$  when we examine the large volume of data such as the ALMA 3D data cubes. Note that our sample does not include the tentative [C II] line detections reported in the ALMA blind line survey (Aravena et al. 2016; Hayatsu et al. 2017), because these tentative [C II] detections have not been spectroscopically confirmed. We identify 16 [C II] line sources in the literature that meet the above criteria. Table 1 summarizes our sample and the references that describe the relevant ALMA observations. In the Appendix, we also list the [C II] line velocity-integrated maps and the spectra for these 16 sources.

In addition to the literature sample, we include new [C II] line detections of two star-forming galaxies, NB816-S-61269 (Ouchi et al. 2008; Fujimoto et al. 2016) and WMH13 (Willott et al. 2013b) at  $z = 5.688$  and  $5.983$ , respectively. In Figure 1, we present the velocity-integrated maps and the spectra for these two [C II] detections. In the velocity-integrated maps of NB816-S-61269 and WMH13, the [C II] line is detected with peak  $S/N$  levels of 5.6 and 5.2, respectively; rest-frame FIR dust continuum emission is not detected from either galaxy. The details of the ALMA observations for these additional sources are listed in Table 1.

From the literature and the additional samples, we obtain a total of 18 [C II] line sources. The 18 [C II] line sources have

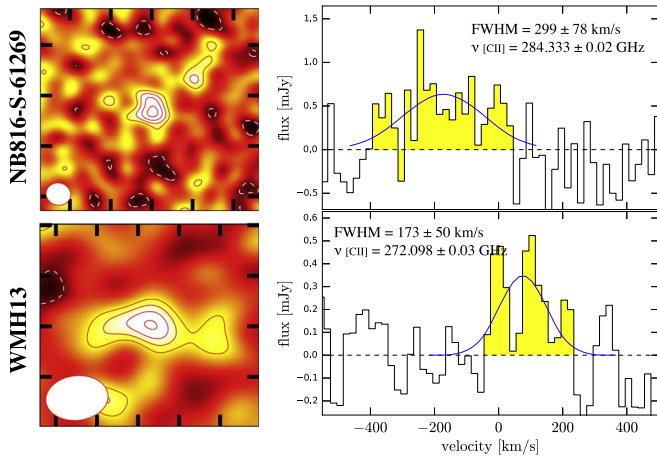


**Figure 1.** New [C II] line detections of NB816-S-61269 (top) and WMH13 (bottom). *Left:* natural-weighted  $4'' \times 4''$  field image of the velocity-integrated [C II] line intensity (moment zero) with contours at the  $-2\sigma$  (white),  $2\sigma$ ,  $3\sigma$ ,  $4\sigma$ , and  $5\sigma$  (red) levels. The ALMA synthesized beams are presented at the bottom left. *Right:* [C II] line spectra with an aperture diameter of  $1''.2$ . The solid curves denote the best-fit profile of the single Gaussian with the best-fit values of the FWHM and the frequency peak. The yellow shaded areas present the integrated velocity ranges for the [C II] line intensity maps in the left panel. The velocities are relative to the  $\text{Ly}\alpha$  line obtained in previous studies (Ouchi et al. 2010; Willott et al. 2013a).

spectroscopic redshifts determined by the [C II] lines ( $z_{[\text{C II}]}$ ) and have absolute rest-frame UV magnitudes ( $M_{\text{UV}}$ ) in the ranges of  $z_{[\text{C II}]} = 5.153\text{--}7.142$  and  $M_{\text{UV}} \simeq -22.8$  to  $-20.4$  ( $\text{SFR} \simeq 10\text{--}70 M_{\odot} \text{ yr}^{-1}$ ). We summarize the physical properties of  $z_{[\text{C II}]}$ ,  $M_{\text{UV}}$ , and the  $\text{Ly}\alpha$  equivalent width ( $\text{EW}_{\text{Ly}\alpha}$ ) in Table 1.

## 2.2. ALMA Data

We reduce the ALMA data for our sample with the Common Astronomy Software Applications package (CASA; McMullin et al. 2007) in the standard manner with the scripts provided by the ALMA observatory. In this process, we carry out recalibrations for the flux density and additional flagging for bad antennae if we find problems in the final images that show striped patterns or significantly higher noise levels than expected. The continuum images and line cubes are produced by the CLEAN algorithm with the TCLEAN task with a pixel scale of  $0''.01$ . For the line cubes, the velocity channel width is rebinned to  $20 \text{ km s}^{-1}$ , where the velocity center is adjusted to the  $\text{Ly}\alpha$  redshift. We do not CLEAN the line cubes because the [C II] line is faint in each  $20 \text{ km s}^{-1}$  channel. The CLEAN boxes were set at the peak pixel positions with  $\text{S/N} \geq 5$  in auto mode, and the CLEAN routines were proceeded down to the  $3\sigma$  level. We list the standard deviation of the pixel values in a final natural-weighted image and a synthesized beam size for the continuum image in Table 1.

Note that the continuum is subtracted from the  $uv$ -data of the line cubes for four sources (Hz4, Hz6, Hz9, and WMH5) whose continuum emission is individually detected (Capak et al. 2015; Willott et al. 2015). The continuum level is estimated from the channels in the velocity range of  $v > |2 \times \text{FWHM}|$  in the same baseband as the [C II] line emission.

## 2.3. HST Data

To study the rest-frame UV properties of our sample, we also use the *HST* Wide Field Camera 3 (WFC3) in F160W,  $1.54 \mu\text{m}$

(*H*-band), images from the Hubble Legacy Archive, where we obtain final flat-field and flux-calibrated science products.

To correct the potential offsets of the *HST* astrometry (e.g., Rujopakarn et al. 2016; Dunlop et al. 2017), we calibrate the astrometry of the *H*-band maps with the *Gaia* Data Release 2 catalog (Gaia Collaboration et al. 2018). First, we identify bright objects in the *H*-band images with SEXTRACTOR version 2.5.0 (Bertin & Arnouts 1996). Second, we cross-match the bright *H*-band objects and the *Gaia* catalog. Finally, we evaluate offsets between the bright *H*-band object centers and the *Gaia* catalog positions. We find that the bright *H*-band object centers indeed have the offsets from the *Gaia* catalog in the range  $\sim 0''.1\text{--}0''.3$ . We correct the astrometry of each *H*-band map to match the *Gaia* catalog based on these offsets. With the above procedure, the majority of our sample shows that the [C II] line and the *H*-band continuum have a consistent peak position within an offset smaller than  $\sim 0''.1$ . However, the large offset over  $0''.5$  still remains in some cases, probably because the astrometry correction does not work successfully, or we witness the intrinsic offset between the [C II] line and the rest-frame UV continuum (e.g., Maiolino et al. 2015). In any case, these objects with the large offsets cause the smearing effect in the stacking results. To securely study the morphological property from the stacking results, we do not include these objects in the following *HST* data analyses. We identify that nine out of 18 sources in our sample have been observed with the *HST/H*-band whose astrometry is successfully corrected. We refer to the nine and the 18 sources as the “ALMA-*HST*” and “ALMA-ALL” samples, respectively. In Table 1, we summarize the *HST* data references and the sources included in the ALMA-*HST* sample.

Note that we confirm that the ALMA astrometry is well consistent with the *Gaia* catalog within a milliarcsecond scale via the bright quasars used as the phase calibrators in the ALMA observations. Thus, we do not carry out any astrometry corrections for our ALMA maps.

## 3. Data Analysis

### 3.1. 3D Position in ALMA Cube

To carry out stacking for the [C II] line and the rest-frame FIR continuum, we estimate source centroids for the 18 [C II] line sources in the ALMA three-dimensional data cubes via the following six steps: (1) We create fiducial [C II] velocity-integrated maps in the velocity range,  $\sim 100\text{--}900 \text{ km s}^{-1}$ , that maximize the S/N level of the [C II] line detection. (2) We measure fiducial positional centroids based on the peak pixel positions (pixel scale =  $0''.01$ ) in the fiducial [C II] velocity-integrated maps, having smoothed them spatially with a  $uv$ -taper of  $0''.6$ . (3) We produce [C II] spectra with an aperture diameter of  $1''.2$  at the fiducial source centroids. (4) We obtain the peak frequencies and FWHMs of the [C II] line emission by fitting a single Gaussian to the [C II] spectra. (5) We recreate velocity-integrated maps with velocity ranges of  $2 \times$  the FWHM. (6) We measure final positional centroids in the new velocity-integrated map in the same manner as step (2). Note that we use the smoothed map (via the  $uv$ -taper) instead of the naturally weighted map in steps (2) and (6) because Monte Carlo simulations in the  $uv$ -visibility plane show that smoothed maps have lower uncertainties in the positional measurements than the intrinsic maps (Fujimoto et al. 2018). We list the final positional centroids and redshifts in Table 1.



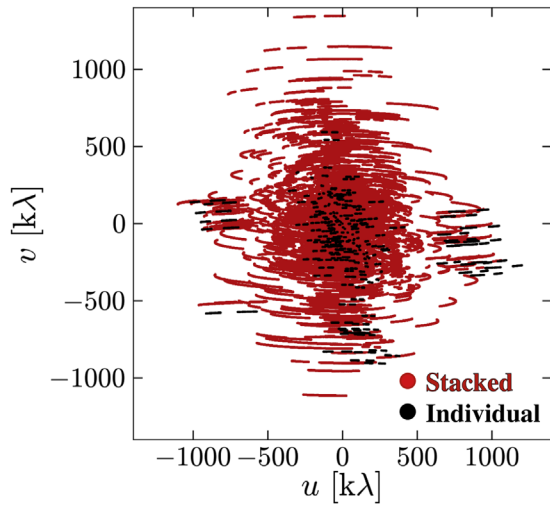


**Figure 2.**  $uv$ -Visibility coverage for individual and stacked data. For the individual data, we present Hz3 data as an example. For the stacked data, the  $uv$ -visibility coverage less than 500 k $\lambda$  is well sampled in circular symmetry, which enables us to investigate the diffuse, extended structures.

### 3.2. ALMA Visibility-based Stacking

We carry out visibility-based stacking for our ALMA data via the following procedure. First, we split the visibility data into the [C II] line and the rest-frame FIR continuum data sets. For the [C II] line data set, we extract the visibility data with the [C II] line channels across a velocity range of 100 km s<sup>-1</sup> ( $=\pm 50$  km s<sup>-1</sup>), where the velocity center is the [C II] frequency peak (the 3D position in our ALMA cubes). We do not adopt a wider velocity range because of the potential contamination of the close companions (Jones et al. 2017; Carniani et al. 2018). For the rest-frame FIR continuum data set, we produce the visibility data whose [C II] line channels in a velocity range of  $2 \times \text{FWHM}$  are fully removed. Second, we shift the coordinate of the visibility data sets by rewriting the source center determined in Section 3.1 as “00:00:00.00 00:00:00.0” with STACKER (Lindroos et al. 2015). Third, we combine the visibility data sets with the CONCAT task. Fourth, we recalculate the data weights for the combined visibility data sets with the STATWT task, based on the scatter of visibilities, which includes the effects of integration time, channel width, and system temperature. Finally, we obtain the stacked data sets of the [C II] line and the rest-frame FIR continuum. The central frequency in the [C II] line data set is 271.167 GHz, which corresponds to the [C II] redshift at  $z = 6.01$ . Assuming the redshift of  $z = 6.01$  as the weighted-average source redshift of our sample, we adopt an angular scale of  $1'' = 5.7$  kpc in the following analyses. Note that we adopt the  $H$ -band peak positions (Section 3.3) as the common stacking centers for the ALMA-*HST* sample.

Figure 2 indicates the  $uv$ -visibility coverage after the visibility-based stacking for the ALMA data sets of the ALMA-ALL sample. For comparison, the  $uv$ -visibility coverage for an individual data set, before stacking, is also plotted. In the stacked data, the  $uv$ -visibility coverage is well sampled, especially for short baselines,  $< 500$  k $\lambda$ , which is important for recovering the flux density from diffuse, extended structures.

In Figure 3, we show the natural-weighted images of the [C II] line and dust continuum after the visibility-based stacking for the ALMA-ALL (ALMA-*HST*) sample, where the standard deviation of the pixel values in the dust continuum image achieves 4.1

(8.3)  $\mu\text{Jy/beam}$  with a synthesized beam size of  $0''.43 \times 0''.36$  ( $0''.74 \times 0.58$ ). The peak pixel S/N ratio shows  $21\sigma$  ( $20\sigma$ ) and  $10\sigma$  ( $8\sigma$ ) significance levels for the [C II] line and dust continuum, respectively, for the ALMA-ALL (ALMA-*HST*) sample. The spatially resolved [C II] line emission in the ALMA-ALL sample is detected at the  $9.3\sigma$  level in the aperture radius of 10 kpc even after masking the emission in a central area up to  $2 \times \text{FWHM}$  of the ALMA synthesized beam, based on the random-aperture method. Because the extended structure is difficult to model by the CLEAN algorithm perfectly, we use the dirty images for both the [C II] line and the rest-frame FIR continuum in the following analyses.

In Figure 4, we present the radial surface brightness profile of the stacked [C II] line and summarize various tests for the extended [C II] line structure. First, we compare our stacking and individual results. In the top left panel of Figure 4, we show the individual results for several [C II] line sources whose lines are detected at high S/N, with an ALMA beam size of  $\gtrsim 0''.8$  to recover the diffuse, extended structures. We find that the stacked results are consistent with the individual results within the scatter, suggesting that our ALMA stacking result provides a faithful representative of the 18 [C II] line sources.

Second, we evaluate the uncertainty of the sample variance. We make 18 newly stacked data sets with 17 [C II] line sources; that is, in each newly stacked data set, we remove one source from the full sample and derive the 18 [C II] radial profiles. In the top right panel of Figure 4, the red shaded area indicates the 16–84th percentiles of these 18 radial profiles. The [C II] radial profile is extended up to a radius of  $\sim 10$  kpc even including the sample variance, suggesting that the sample variance does not change our results for the existence of the extended [C II] line emission. Third, we investigate whether the extended [C II] line structure is caused by any specific data properties. We remove the sources that are (I) taken with the lowest resolutions (BDF2203, NTTDF6345, and WMH13) and (II) reported to have companions (WMH5, Hz2, Hz6, and Hz8; Jones et al. 2017; Carniani et al. 2018) and obtain newly stacked data. In the top right panel of Figure 4, we present the radial profiles of the [C II] line emission in the newly stacked data. We find that the newly stacked [C II] line profiles reproduce extended structures that are well consistent with the original stacking result in the ALMA-ALL sample. This indicates that the extended [C II] line structure is not caused either by the bias to the low-resolution data or the contamination of the companions. Fourth, we examine the surface brightness dimming effect in our sample. We divide the 18 [C II] line sources into two subsamples, low-redshift ( $z < 6$ ) and high-redshift ( $z > 6$ ) samples, and obtain other newly stacked data. In the bottom left panel of Figure 4, we show the radial profiles of the [C II] line emission in both subsamples. We find that the [C II] line profiles in both subsamples reproduce the extended structures that have good agreement with the original stacking result in the ALMA-ALL sample. This suggests that the surface brightness dimming effect does not significantly affect our stacking results. Fifth, we compare the structures of the [C II] line and the dust continuum in the same significance level. We produce a random noise map smoothed by the ALMA beam and combine the noise and the stacked [C II] line maps. Changing the noise levels, we obtain the noise-enhanced [C II] line map, whose peak S/N becomes comparable to the dust continuum one. We create 50 noise-enhanced [C II] line maps. In the bottom right panel of Figure 4, we show the 16–84th

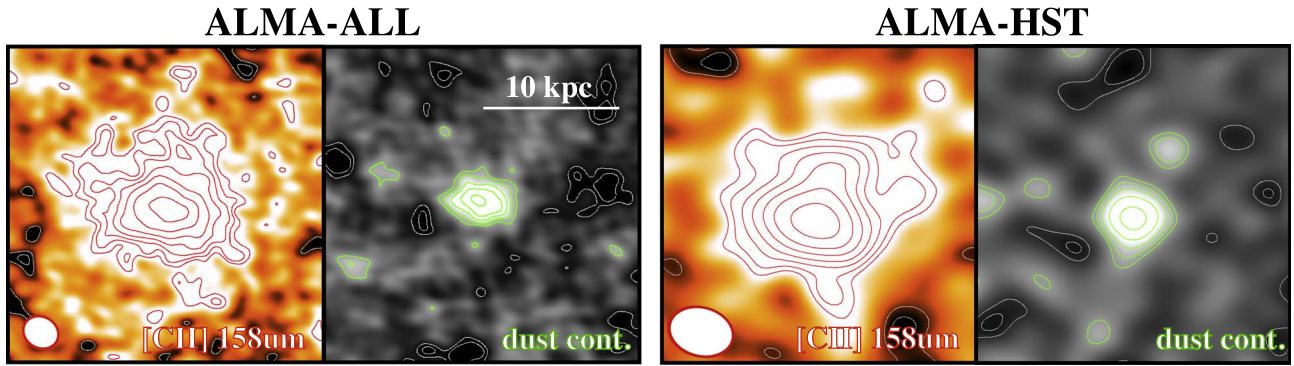


**Figure 3.** Natural-weighted  $4'' \times 4''$  field image after the visibility-based stacking of the [C II] line and the dust continuum for the ALMA-ALL (left) and ALMA-*HST* (right) samples. The red and green contours denote the  $2, 2\sqrt{2}, 4, \dots \times \sigma$  levels of the [C II] line and the dust continuum emission, while the white contours indicate the  $-2\sigma$  and  $-2\sqrt{2}\sigma$  levels. The synthesized beams are presented at the bottom left in each panel.

percentile of the [C II] radial profile in the noise-enhanced maps. We find that the [C II] line profile still exceeds more than the dust continuum in these noise-enhanced maps, showing that the different structures between the [C II] line and the dust continuum are not mimicked by the difference in the dynamic range.

### 3.3. *HST/H-band Stacking*

We have performed image-based stacking for the ALMA-*HST* sample, exploiting their deep archival *HST* *H*-band imaging. Before stacking, we carry out the following procedure: (1) We cut out  $8'' \times 8''$  stamps from the *H*-band images around the [C II] line sources, and we set the pixel scale to  $0''.01$ , which corresponds to our ALMA images. (2) We identify low-redshift contaminants within  $2''.0$  from the [C II] sources, by cross-matching the [C II] line source positions with photometric redshift catalogs (Ilbert et al. 2013; Skelton et al. 2014). (3) We remove the low-redshift contaminants from the *H*-band images by fitting Sérsic profiles (Sérsic 1963) with GALFIT (Peng et al. 2010). We then proceed to generate an average stack, weighted by the noise levels of the ALMA images of the [C II] line source. This is because the visibility-based stacking for our ALMA data is weighted by the visibility scatter, which generally corresponded to the noise levels on the ALMA images.

In panel (f) of Figure 5, we show the stacked *H*-band image for the ALMA-*HST* sample. In the *HST* stacking, we adopted stacking centroids defined by the peak positions of the *H*-band images, smoothed with the *uv*-tapered ALMA beams in a manner consistent with the [C II] line stacking.

To directly compare the size and morphology of the *HST* and ALMA images, we need to convolve the *HST* image to obtain a point-spread function (PSF) that resembles the one of the ALMA image. We use GALFIT to obtain a kernel with which the *H*-band PSF can be converted to the ALMA beam. For the kernel, we assume a sum of three independent Sérsic profiles whose positions are fixed at the center.

In Figure 5, we present a schematic overview of converting the *H*-band PSF to the ALMA beam with the best-fit kernel. We first convolve the *HST* PSF (panel a) with the best-fit kernel (panel b) and derive the mock ALMA beam (panel c). We then subtract the actual ALMA beam (panel d) from the mock ALMA beam and produce the residual map (panel e). Within a radius of  $1''.0$  on the residual map, we find that the differences between the mock and actual ALMA beams are less than

$\sim 1.8\%$ , showing that the best-fit kernel reproduces the ALMA beams well from the *H*-band PSF. We finally apply the convolution to the stacked *H*-band image (panel f) with the best-fit kernel, and we obtain the mock *H*-band image whose PSF is almost the same as the stacked ALMA image.

## 4. Results

### 4.1. Discovery of [C II] Halo

Figure 6 presents the radial surface brightness profiles of the [C II] line, rest-frame FIR, and UV continuum, derived from the stacking results for the ALMA-*HST* (circles) and ALMA-ALL (squares) samples. For a fair comparison, the ALMA-*HST* results are obtained by reperforming the ALMA visibility-based stacking with the *HST/H*-band peak positions, while the ALMA-ALL results are not, due to the lack of the *HST/H*-band images.

In Figure 6, the ALMA-ALL and ALMA-*HST* results show good agreement in profiles of both the [C II] line and the rest-FIR continuum. We find that the radial profile of the [C II] line emission is extended up to a radius of  $\sim 10$  kpc, which contrasts with the rest-frame UV and FIR continuum. Because the typical effective radius of the normal star-forming galaxies at  $z \sim 6$  is estimated to be less than 1 kpc (e.g., Shibuya et al. 2015), the  $\sim 10$  kpc scale structure at this epoch corresponds to the circumgalactic medium (CGM) surrounding the galaxies. These results suggest that the [C II] line emission is produced in the wide CGM areas even without stellar continuum. We discuss the physical origin of the [C II] halo in Section 5.

We also find that the profiles of the rest-frame FIR and UV continuum are consistent within the  $1\sigma$  errors. Note that the rest-frame FIR continuum is likely to follow the ALMA beam, while the rest-frame UV continuum is slightly resolved with the ALMA beam. This suggests that the intrinsic size of the rest-frame FIR continuum is smaller than that of the rest-frame UV continuum, which is consistent with the recent ALMA results of the compact rest-frame FIR size more than the rest-frame UV and optical sizes among the star-forming galaxies at  $z \sim 2-4$  (e.g., Ikarashi et al. 2015; Simpson et al. 2015; Hodge et al. 2016; Fujimoto et al. 2017, 2018).

### 4.2. Effect of [C II]–UV Offset

Recent studies report a possibility that [C II] line emitting regions are physically offset from the rest-frame UV ones (e.g., Maiolino et al. 2015). To evaluate the potential effect from the

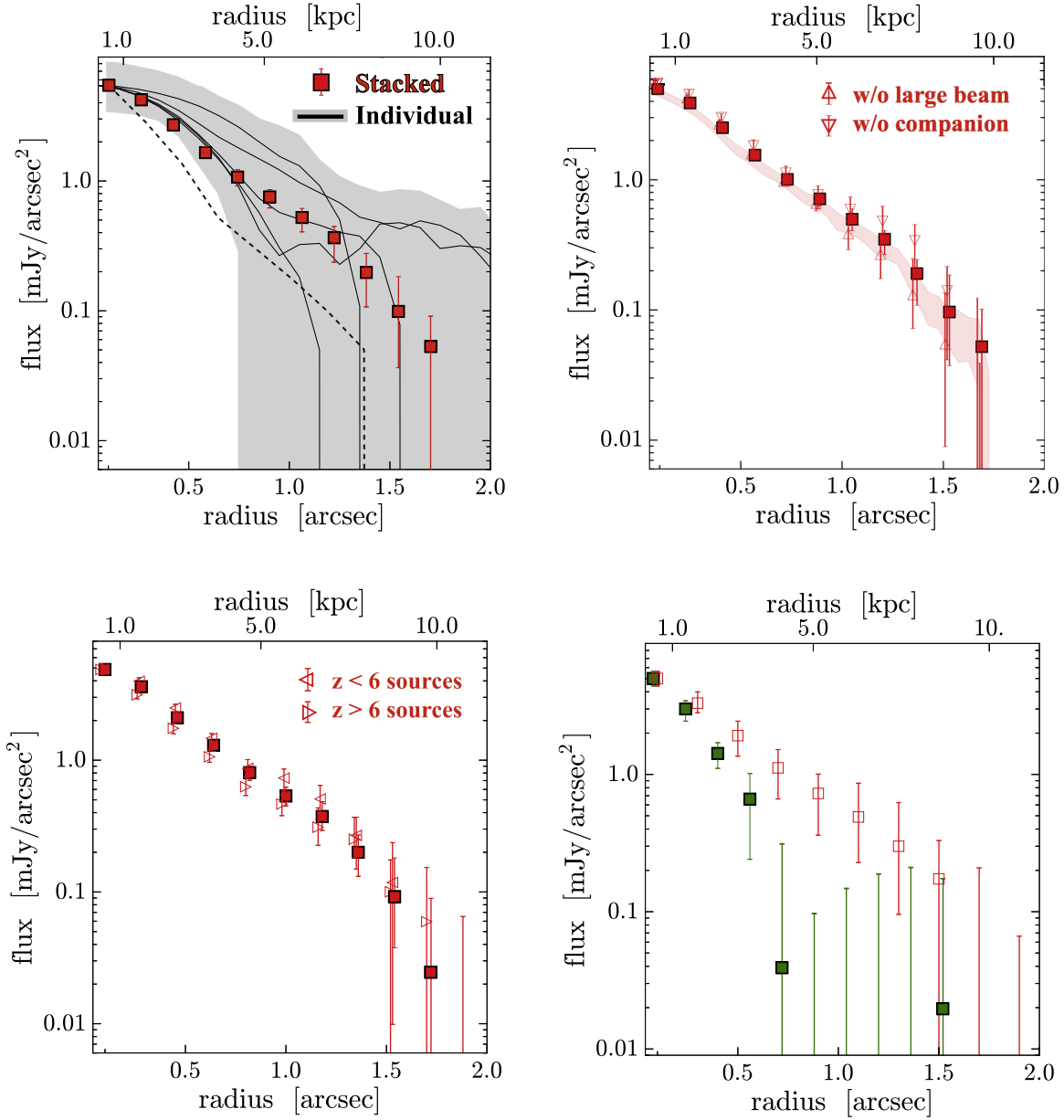


**Figure 4.** Radial surface brightness profile of the [C II] line (red filled squares) and dust continuum (green filled squares) emission for the ALMA-ALL sample. Top left: black solid curves denote the individual results from five [C II] line sources whose [C II] lines are detected with high S/N levels and with the ALMA beam sizes of  $\gtrsim 0''.8$  to recover the diffuse, extended structures. The gray shaded areas indicate the error range of the individual results. The black dashed curve presents the synthesized ALMA beam in the ALMA-ALL sample. Top right: the red shaded area shows the 16–84th percentile of the sample variance (see the text). The open symbols indicate the restacked results without the [C II] line sources that are (1) taken with the lowest resolutions (BDF2203, NTTDF6345, and WMH13; upward triangle) and (2) reported to have companions (WMH5, Hz2, Hz6, and Hz8; downward triangle). Bottom left: the restacked results for the low-redshift ( $z < 6$ ; leftward triangle) and high-redshift ( $z > 6$ ; rightward triangle) subsamples among the 18 [C II] line sources. Bottom right: those whose peak S/N ratio is reduced down to the level comparable to the dust continuum map. All radial profiles are normalized to the peak value of the [C II] line.

[C II]–UV offsets in our results, we perform the ALMA and *HST* stacking for the ALMA-*HST* sample by adopting two different stacking centers: the *HST*/*H*-band and ALMA [C II] line peak positions, and compare the radial profiles from these stacking results.

In Figure 7, the circle and cross symbols represent the stacking results derived with the common stacking centers of the *HST*/*H*-band continuum and ALMA [C II] line peak positions, respectively. We find that the [C II] line profile is extended more than both the rest-frame FIR and UV continuum profiles in any case. This suggests that the [C II] line originates from much wider regions than the continuum emission at rest-frame FIR and UV

wavelengths, and clearly shows that the extended structure of the [C II] line is not caused by the [C II]–UV offsets.

#### 4.3. Radial Ratio of $L_{[\text{C II}]}$ to Total SFR

To test whether the extended [C II] line structure is caused by satellite galaxies, we investigate radial values of the [C II] line luminosity  $L_{[\text{C II}]}$  at a given SFR derived from the rest-frame FIR and UV continuum. Because the ALMA-ALL and ALMA-*HST* results are consistent with each other (Figure 6), we adopt the rest-frame UV results from the ALMA-*HST* sample and use the [C II] line and rest-frame FIR continuum results from the



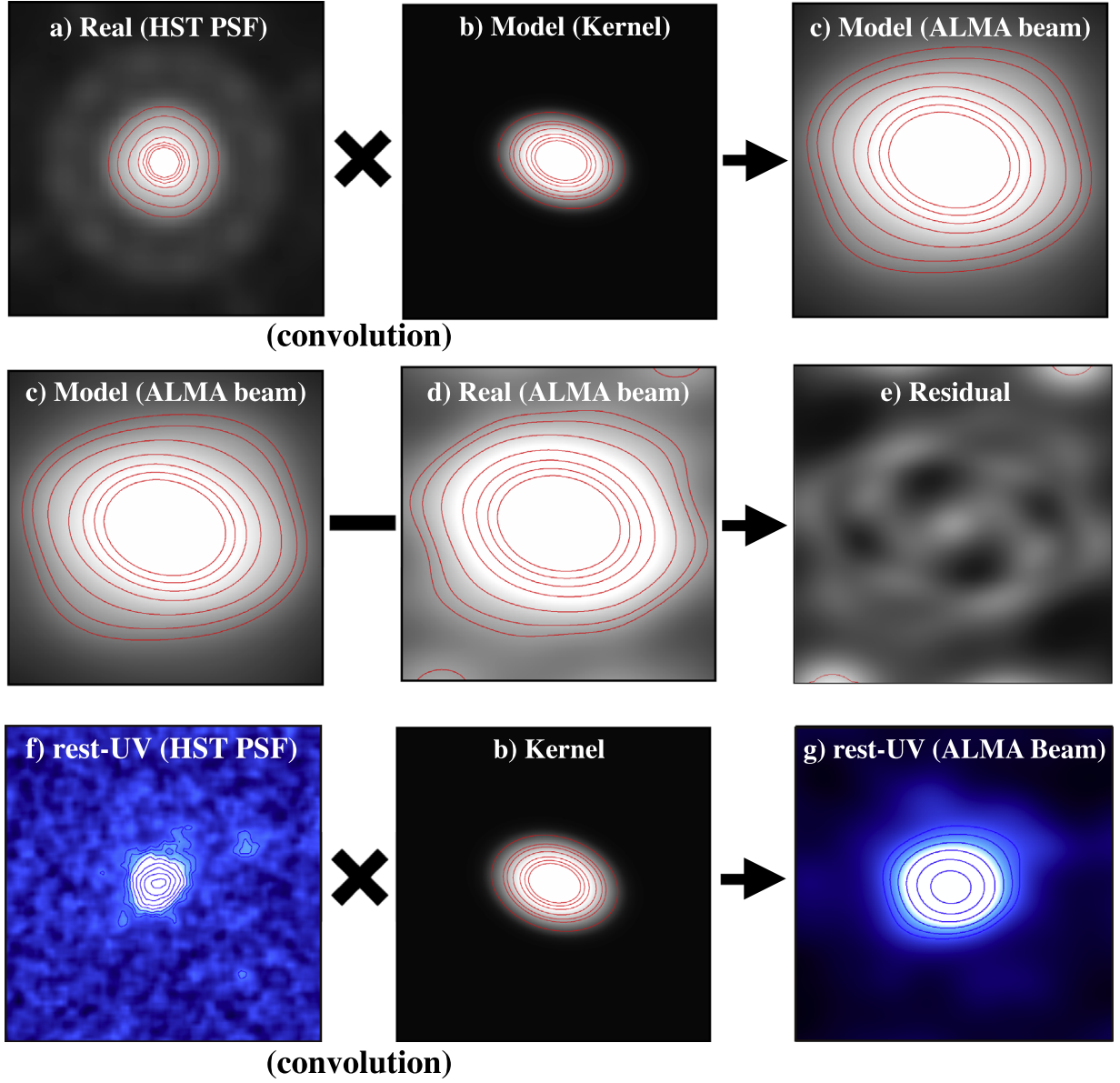


**Figure 5.** Schematic overview to obtain the mock *HST*/*H*-band image whose spatial resolution is matched to the stacked ALMA image for the ALMA-*HST* sample: (a) *HST*/*H*-band point-spread function, (b) best-fit kernel composed of three Sérsic profiles obtained with GALFIT, (c) best-fit ALMA beam model obtained with GALFIT, (d) synthesized beam in the stacked ALMA image for the ALMA-*HST* sample, (e) residual between (c) and (d), (f) stacked *HST*/*H*-band image for the ALMA-*HST* sample, and (g) stacked *HST*/*H*-band image obtained by convolving (f) with (b). The red contours represent 3%, 5%, 10%, 20%, 30%, 40%, and 50% of the PSF or beam response. The blue contours denote the  $2, 2\sqrt{2}, 4, \dots \times \sigma$  levels of the rest-frame UV continuum emission. The cutout sizes are  $2'' \times 2''$  and  $4'' \times 4''$  for the panels (a)–(e) and (f)–(g), respectively.

ALMA-ALL sample to reduce the errors in the following estimates.

We first estimate the radial  $L_{[\text{C II}]}$  value. For our sources, the weighted-average source redshift and FWHM of the [C II] line width are estimated to be  $z = 6.01$  and  $270 \text{ km s}^{-1}$ , respectively. Since the velocity-integrated width is  $100 \text{ km s}^{-1}$  in the stacked [C II] line map, we correct the velocity-integrated value in the range from 100 to  $270 \text{ km s}^{-1}$ , assuming a single Gaussian line profile, to recover the total value of  $L_{[\text{C II}]}$ . We next evaluate the radial SFR value. We derive the obscured ( $\text{SFR}_{\text{IR}}$ ), unobscured ( $\text{SFR}_{\text{UV}}$ ), and total SFR ( $\text{SFR}_{\text{total}}$ ) with the equations in Murphy et al. (2011), as follows:

$$\text{SFR}_{\text{IR}} [M_{\odot} \text{ yr}^{-1}] = 3.88 \times 10^{-10} L_{\text{IR}} [\text{erg s}^{-1}], \quad (1)$$

$$\text{SFR}_{\text{UV}} [M_{\odot} \text{ yr}^{-1}] = 4.42 \times 10^{-10} L_{\text{UV}} [\text{erg s}^{-1}], \quad (2)$$

$$\text{SFR}_{\text{total}} = \text{SFR}_{\text{IR}} + \text{SFR}_{\text{UV}}, \quad (3)$$

where  $L_{\text{IR}}$  is the integrated IR flux density estimated using a typical modified blackbody whose spectral index  $\beta_d$  and dust temperature  $T_d$  are  $\beta_d = 1.8$  (Planck Collaboration et al. 2011) and  $T_d = 35 \text{ K}$  (Coppin et al. 2008), and  $L_{\text{UV}}$  is the rest-frame UV luminosity at  $0.16 \mu\text{m}$  with the *HST* *H*-band. Finally, we divide the radial  $L_{[\text{C II}]}$  values by the radial SFR values and obtain the radial ratio of  $L_{[\text{C II}]} / \text{SFR}_{\text{total}}$ .

In Figure 8, we show the surface densities of  $L_{[\text{C II}]}$  ( $\Sigma_{L_{[\text{C II}]}}$ ) and  $\text{SFR}_{\text{total}}$  ( $\Sigma_{\text{SFR}}$ ) as a function of radius (middle panel), and the radial ratio of  $L_{[\text{C II}]} / \text{SFR}_{\text{total}}$  (right panel) as a function of  $\text{SFR}_{\text{total}}$  for our stacking results. For comparison, the right

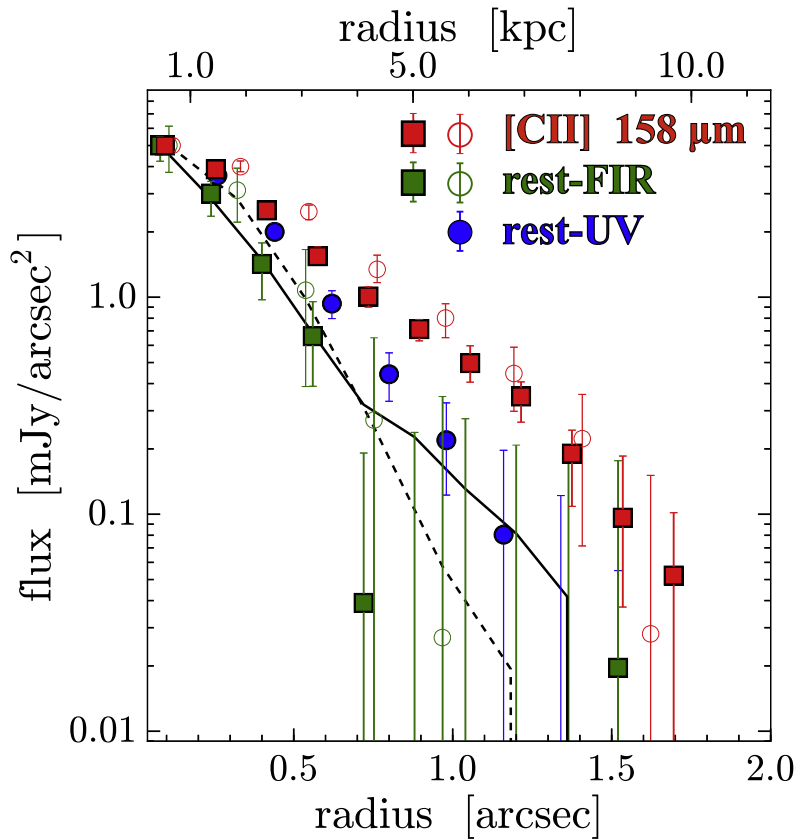


**Figure 6.** Radial surface brightness profiles for the ALMA-*HST* (circles) and ALMA-ALL (squares) samples. The radial values are estimated by the median of each annulus. The red, green, and blue symbols denote the [C II] line, rest-frame FIR, and rest-frame UV continuum emission. The rest-frame UV continuum profile is directly derived from the mock *HST*/*H*-band image, whose resolution is matched to that of the ALMA image. The black dashed and solid curves denote the ALMA synthesized beams in the stacked images of the ALMA-*HST* and ALMA-ALL samples, respectively. All radial profiles are normalized to the peak value of the [C II] line. The green and red symbols are slightly shifted along the *x* axis for clarity.

panel of Figure 8 also presents global-scale  $L_{[\text{C II}]} / \text{SFR}_{\text{total}}$  ratios of the local dwarf galaxies (De Looze et al. 2014).

In the right panel of Figure 8, the red filled and open circles denote our stacking results in the outer (radius of  $\geq 4$  kpc) and central ( $< 4$  kpc) regions, respectively. We find that  $L_{[\text{C II}]} / \text{SFR}_{\text{total}}$  decreases with  $\text{SFR}_{\text{total}}$ . The highest ratios ( $> 10^8 L_{\odot} M_{\odot}^{-1} \text{ yr}$ ) are found at the outer regions and are not compatible with typical values found in the local dwarf galaxies ( $< 3 \times 10^7 L_{\odot} M_{\odot}^{-1} \text{ yr}$ ; black dots in the figure). These results indicate that the [C II] halo is not likely driven by satellite galaxies. Note that other types of high-*z* galaxies with  $\text{SFR}_{\text{total}} > 10 M_{\odot}$ , such as star-forming, submillimeter, and quasar-host galaxies, show ratios of  $10^6 \sim 10^7 L_{\odot} M_{\odot}^{-1} \text{ yr}$  (e.g., Capak et al. 2015; Rybak et al. 2019; Venemans et al. 2019), with which it is yet difficult to explain the highest ratios in our stacking results ( $> 10^8 L_{\odot} M_{\odot}^{-1} \text{ yr}$ ).

Díaz-Santos et al. (2014) report the [C II] line emission extended over an  $\sim 1\text{--}10$  kpc scale around LIRGs, and we also compare our results with this spatially resolved data. In the right panel of Figure 8, we show the  $L_{[\text{C II}]} / \text{SFR}_{\text{total}}$  ratios of the extended emission around local LIRGs. We find that the highest ratios in our stacking results ( $> 10^8 L_{\odot} M_{\odot}^{-1} \text{ yr}$ ) are still higher than those around the local LIRGs ( $< 3 \times 10^7 L_{\odot} M_{\odot}^{-1} \text{ yr}$ ; green crosses in the figure). The [C II] halo at  $z \sim 6$  is thus not identical to the extended [C II] line emission observed in the local universe, which may suggest that [C II] halos evolve with redshift. We discuss possible origins of the [C II] halo in Section 5.

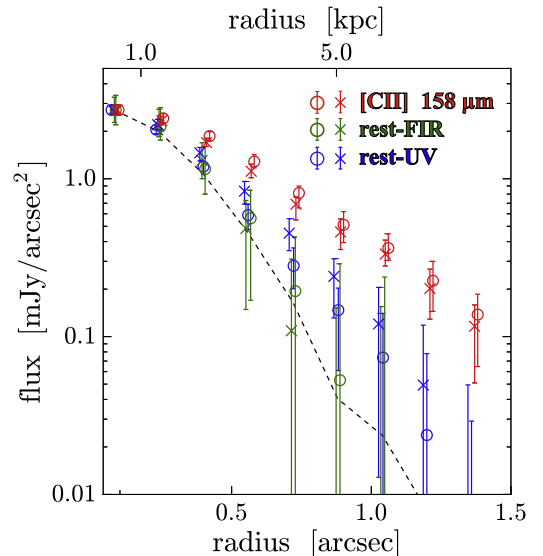


**Figure 7.** Radial surface brightness profiles for the ALMA-*HST* sample derived with different stacking centers. The red, green, and blue symbols denote the [C II] line, rest-frame FIR, and rest-frame UV continuum emission. The color crosses and circles are the stacking results based on the stacking centers of the [C II] line and the *HST*/*H*-band peak positions, respectively. The rest-frame UV continuum profile is directly derived from the mock *HST*/*H*-band image, whose resolution is matched to the ALMA image. The black dashed curve denotes the ALMA synthesized beam. All radial profiles are normalized to the peak value of the [C II] line. The green and red symbols are slightly shifted along the *x* axis for clarity.



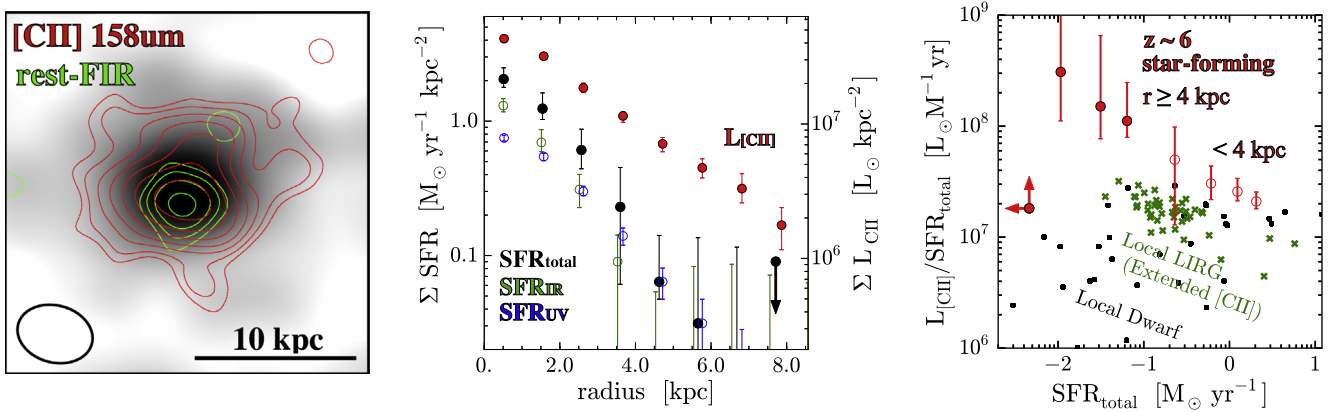


**Figure 8.** Left: rest-frame UV emission of the ALMA-*HST* sample in the *HST*/*H*-band  $4'' \times 4''$  image whose resolution is matched to the ALMA image. The red and green contours denote the  $2, 2\sqrt{2}, 4, \dots \times \sigma$  levels of the [C II] line and the dust continuum emission, respectively. The ALMA synthesized beam is presented at the bottom left. Middle: radial profiles of  $\Sigma_{\text{SFR}}$  (left axis) and  $\Sigma_{L_{\text{[C II]}}}$  (right axis). The blue, green, and black circles indicate  $\Sigma_{\text{SFR}_{\text{UV}}}$ ,  $\Sigma_{\text{SFR}_{\text{FIR}}}$ , and  $\Sigma_{\text{SFR}_{\text{total}}}$ , respectively, based on Equations (1)–(3). The red circles denote  $\Sigma_{L_{\text{[C II]}}}$  normalized to  $\Sigma_{\text{SFR}}$  with the ratio of  $L_{\text{[C II]}}/\text{SFR}_{\text{total}} = 10^7 [L_{\odot} M_{\odot}^{-1} \text{yr}]$ , which is the average value in the local star-forming galaxies (De Looze et al. 2014). Right: ratio of  $L_{\text{[C II]}}/\text{SFR}_{\text{total}}$  as a function of  $\text{SFR}_{\text{total}}$ . The filled (open) red circles indicate our stacking results at a radius of  $\geq 4$  kpc ( $< 4$  kpc). The black dots denote local dwarf galaxy results in the global scale reported in De Looze et al. (2014). The green crosses present the extended [C II] line emission calculated from the local luminous infrared galaxy (LIRG) results in Díaz-Santos et al. (2014). We assume an area of  $1 \text{ kpc}^2$  for the  $L_{\text{[C II]}}$  and  $\text{SFR}_{\text{total}}$  estimates in our stacking and the local LIRG results. At the radius of  $> 7$  kpc, the  $\text{SFR}_{\text{total}}$  value in our stacking results becomes negative because of the noise fluctuations on the low surface brightness of the rest-frame UV and FIR continuum emission, where we evaluate the lower limit of the ratio by using the upper limit of  $\text{SFR}_{\text{total}}$ .

#### 4.4. Scale Length of [C II] Halo

We characterize the detailed radial surface brightness profile of the [C II] line emission by two-component fitting with GALFIT. Here we assume the two components to be the central and the halo components.

For the central component, we adopt the Sérsic profile whose parameters are estimated from the rest-frame UV profile in the stacked *HST*/*H*-band image (Figure 5(f)). We obtain the best-fit effective radius  $r_e$  and the Sérsic index  $n$  of  $r_e = 1.1 \pm 0.1 \text{ kpc}$  and  $n = 1.2 \pm 0.01$ , which are consistent with the average values estimated from the normal star-forming galaxies at  $z \sim 6$  (Shibuya et al. 2015). For the halo component, we utilize the exponential profile. The exponential profile has been used for scale-length measurements of the Ly $\alpha$  halo, which is universally identified around the high- $z$  star-forming galaxies (e.g., Steidel et al. 2011; Matsuda et al. 2012; Momose et al. 2014, 2016; Leclercq et al. 2017). The exponential profile is described as  $C_n \exp(-r/r_n)$ , where  $C_n$  is a constant and  $r_n$  is the scale length. We fix the central positions of both the central and halo components to obtain a stable result.

The top panel of Figure 9 presents the best-fit results with the Sérsic+exponential profiles for the [C II] line emission. We obtain the best-fit scale-length values of  $r_n = 3.3 \pm 0.1 \text{ kpc}$ . This corresponds to a best-fit effective radius of  $r_e = 5.6 \pm 0.1 \text{ kpc}$ , showing that the [C II] halo is extended  $\sim 5$  times more than the stellar continuum in the central galactic component. Note that the visibility-based profile fitting with UVMULTIFIT (Martí-Vidal et al. 2014) also provides us with a best-fit value of  $r_e = 5.1 \pm 1.7 \text{ kpc}$  for the halo component, which is consistent with the GALFIT result within the error.

In Figure 9, we compare the radial surface brightness profiles of the [C II] with the Ly $\alpha$  halos universally identified in the normal star-forming galaxies at  $z \sim 3$ –6 (e.g., Momose et al. 2016; Leclercq et al. 2017). For the [C II] line emission, we adopt the result from the ALMA-ALL sample, due to the high significance detection. For the Ly $\alpha$  line emission, we use the recent results with the deep MUSE data for the high- $z$  Ly $\alpha$

emitters (LAEs) of Leclercq et al. (2017), where the authors estimate the best-fit radial surface brightness profiles by fitting the two-component Sérsic+exponential profile. We select the best-fit results of six LAEs at  $z > 5$  with  $M_{\text{UV}} \lesssim -21 \text{ mag}$  and  $\text{EW}_{\text{Ly}\alpha} < 100 \text{ \AA}$  that are consistent with the parameter space of our sample (Table 1). We find that the radial surface brightness profile of the [C II] line emission is comparable to that of the Ly $\alpha$  line emission. The median  $r_n$  value for the six LAEs is estimated to be  $3.8 \pm 1.7 \text{ kpc}$ , which is consistent with our best estimate of  $3.3 \pm 0.1 \text{ kpc}$ . These results may imply that the physical origin of the extended [C II] line emission is related to the Ly $\alpha$  halo.

Note that we confirm that it is hard to reproduce the extended morphology of the [C II] line emission with the central component alone. In the bottom panel of Figure 9, we present the residuals of the [C II] line emission obtained from the best-fit results of the one- (central) and two-component (central +halo) fittings with UVMULTIFIT. We find that the residuals in the one-component fitting result show a bump at a radius of  $\sim 1''$  over the errors, while the residuals in the two-component fitting result are broadly consistent with zero. This suggests that the extended morphology of the [C II] line emission consists of a combination of the central plus halo components.

#### 4.5. [C II] Stacked Spectrum

We also perform the stacking for the [C II] line spectra of the ALMA-ALL sample to test whether our ALMA sample has a broad wing feature, which is a good probe of ongoing outflow activities. For the stacking procedure, we adopt the same manner as previous ALMA studies (Bischetti et al. 2019; Decarli et al. 2018). Here we adopt a relatively small aperture diameter of  $0''.4$  for the individual spectra to reduce contamination by close companions (Jones et al. 2017; Carniani et al. 2018).

In Figure 10, we show the stacked [C II] line spectrum with the best-fit two Gaussian component model: the combination of the core and broad components whose velocity centers are fixed at  $0 \text{ km s}^{-1}$  for the stable results. The best-fit FWHMs are

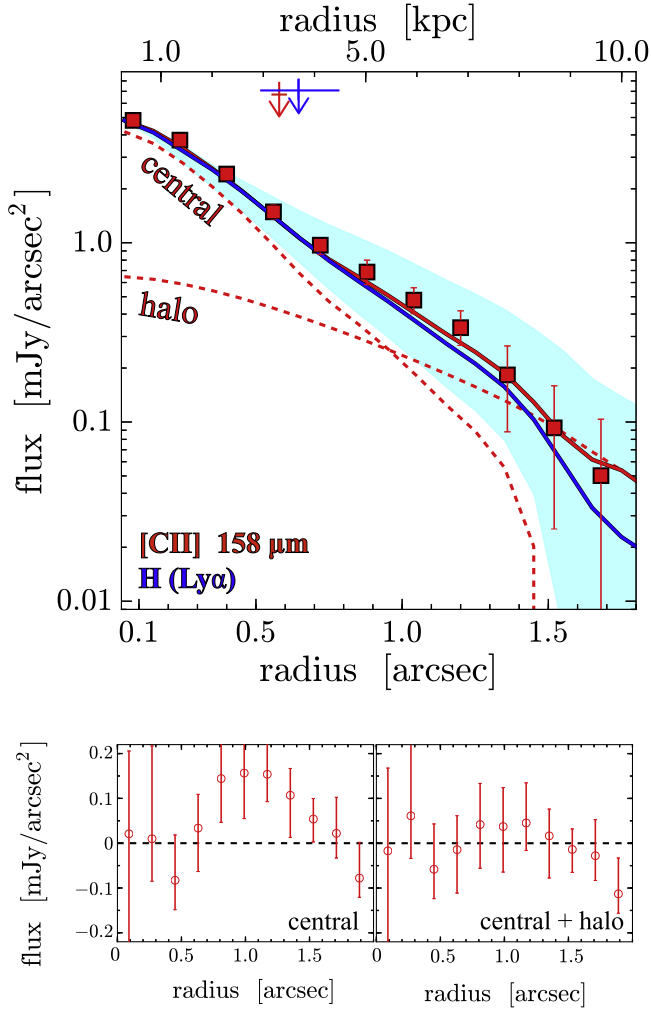


**Figure 9.** Top: two-component Sérsic+exponential profile fitting for the [C II] line, averaged over 18 galaxies. The red dashed curves represent the best-fit results of the central stellar continuum and outer halo components, while the solid red curve denotes the sum of the best-fit two-component profiles. The solid blue curve and the shaded region indicate the median and the 16–84th percentile of the radial surface brightness profile of the Ly $\alpha$  lines in a recent control sample from MUSE (Leclercq et al. 2017). For the Ly $\alpha$  line, we convolve the best-fit results of the Sérsic+exponential profiles with the ALMA beam. The red and blue arrows with error bars show the best-fit scale lengths of the [C II] and Ly $\alpha$  halo components, respectively. Bottom: residuals in the best-fit results of one- (left) and two-component (right) profile fittings.

estimated to be  $296 \pm 40 \text{ km s}^{-1}$  and  $799 \pm 654 \text{ km s}^{-1}$  for the core and broad components, respectively. In the velocity range  $\pm 400\text{--}800 \text{ km s}^{-1}$ , the velocity-integrated intensity is tentatively detected at the  $3.2\sigma$  level. Moreover, Sugahara et al. (2019) have recently reported that the rest-frame UV metal absorption lines are blueshifted by the central outflow velocity of  $440^{+110}_{-140} \text{ km s}^{-1}$  from the [C II] systemic redshift in the stacked Keck spectra, whose stacking sample includes six out of our 18 [C II] line sources. These results may suggest that the tentative broad wing feature is produced by the outflow.

Note that there are other possibilities that produce the broad wing feature. One possibility is contamination of the satellite galaxies. The [C II] line emission from the individual satellite galaxies can be smoothed in the stacking procedure for the 18 galaxies, which may be identified as the broad wing feature.

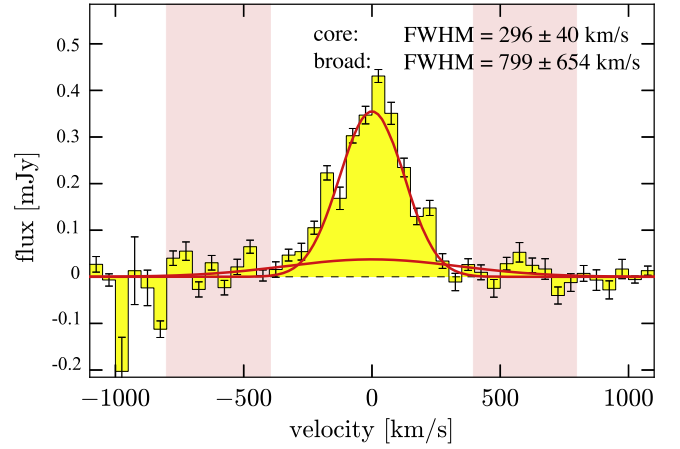


**Figure 10.** ALMA [C II] line spectrum averaged over the ALMA-ALL sample. The spectrum is derived with an aperture diameter of  $0''.4$ . The red curves denote the best-fit two (core + broad) Gaussian component model. The shaded regions indicate the velocity ranges in which the velocity-integrated intensity is tentatively detected at the  $3.2\sigma$  level.

Another possibility is that the faint continuum emission is mistakenly identified as the broad wing feature. Although we have performed the continuum subtraction for the [C II] line data cubes of the four galaxies whose continuum emission is individually detected, it is possible that the faint continuum emission from the rest of the 14 ( $= 18 - 4$ ) galaxies appears in the deeply stacked spectrum. Since the significance of the broad wing is low, we cannot draw definite conclusions from our data.

#### 4.6. Comparison with Model

We compare our observational results with two independent numerical simulations for star-forming galaxies with halo mass  $M_{\text{halo}} \sim 10^{11}\text{--}10^{12} M_{\odot}$  at  $z \sim 6$ . Note that our sample is characterized by an average  $M_{\text{UV}}$  value of  $\lesssim -21$  mag (Table 1) which corresponds to  $M_{\text{halo}} \approx 10^{11}\text{--}10^{12} M_{\odot}$  from the  $M_{\text{UV}}\text{--}M_{\text{halo}}$  relation (Harikane et al. 2018).

The first set is a zoom-in simulation for the star-forming galaxy Althæa (Pallottini et al. 2017a, 2017b; Behrens et al. 2018). The hydrodynamical and dust radiative transfer (RT) simulations are combined, which provides realistic predictions for the spatial distribution of the [C II] line as well as the rest-frame FIR and UV continuum emission, with a spatial resolution of 30 pc. The hydrodynamical and dust RT simulations are fully described in previous studies (Pallottini et al. 2017a, 2017b; Behrens et al. 2018). Note that the dust RT is calculated as a postprocessing step on snapshots of the hydrodynamical simulation. The [C II] line emission is computed in postprocessing (Vallini et al. 2015) by adopting the photoionization code CLOUDY (Ferland et al. 2017). In these processes, cosmic microwave background (CMB) suppression (da Cunha et al. 2013; Pallottini et al. 2015; Zhang et al. 2016; Lagache et al. 2018) is included in the calculation.

The second set is another cosmological hydrodynamic zoom-in simulation performed by the smoothed particle hydrodynamics (SPH) code GADGET-3 (Springel 2005) with the subgrid models developed in the *Overwhelmingly Large Simulations* project (Schaye et al. 2010) and the *First Billion Year* (FiBY) project (e.g., Johnson et al. 2013), which reproduce the general properties of the high-redshift galaxy

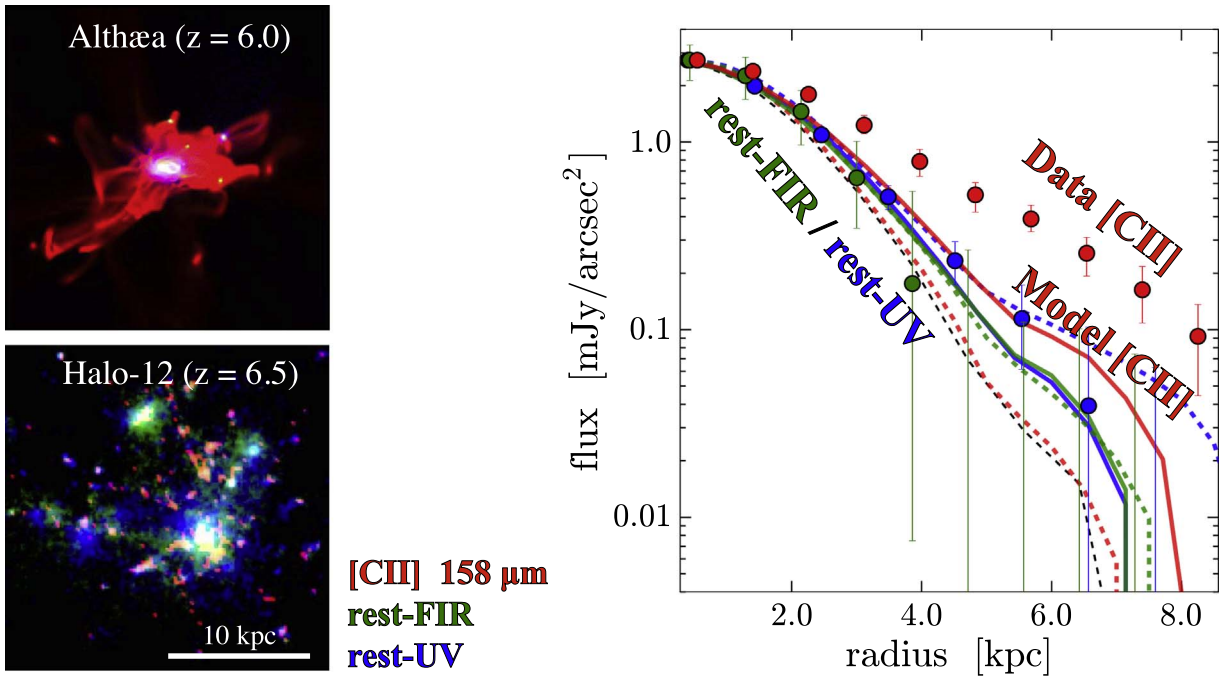


**Figure 11.** Left:  $4'' \times 4''$  fake-color image for Althæa at  $z = 6.0$  (top) and Halo-12 (bottom) in the zoom-in simulations (red: [C II] line, green: rest-frame FIR continuum, blue: rest-frame UV continuum). Right: radial surface brightness profiles of the [C II] line (red curve), rest-frame FIR (green curve), and UV (blue curve) continuum emission estimated in the zoom-in simulations via a stacking procedure. The solid and dashed color lines represent the Althæa and Halo-12 results, respectively. The black dashed curve denotes the ALMA synthesized beam. The circles indicate the ALMA-*HST* stacking results, whose colors are assigned in the same manner as in the left panel.

population well (e.g., Cullen et al. 2017). For this comparison, we use four different halos: Halo-12, Halo-A, Halo-B, and Halo-C, which have  $M_{\text{halo}} = (0.5-1) \times 10^{12} M_{\odot}$  at  $z = 6.2-6.5$ . The details of Halo-12 are discussed in Yajima et al. (2017) and Arata et al. (2019a, 2019b), but the latter three halos are newly simulated for this paper with similar initial conditions but with different merger histories. The minimum gravitational softening length is  $\epsilon_g = 200$  pc (comoving), so we achieve  $\sim 25$  pc resolution at  $z = 7$  for gravity. We also allow the SPH smoothing length to be adaptive down to 10% of  $\epsilon_g$ , so the hydrodynamic resolution reaches several parsecs at  $z = 6-7$ . The RT calculation including the dust absorption/re-emission is performed as a postprocess with “All-wavelength Radiative Transfer with Adaptive Refinement Tree” (ART<sup>2</sup> code; Li et al. 2008; Yajima et al. 2012). This calculation provides the spectral energy distribution (SED) over a wide wavelength range and solves for the ionization structure of the ISM/CGM. The [C II] line emissivity is estimated from the ionized carbon abundance. The details of hydrodynamic simulations, RT, and the [C II] line computations are fully described in Yajima et al. (2017), Arata et al. (2019b), and S. Arata et al. (2019, in preparation).

The left panel of Figure 11 presents a color composite of the [C II] line, rest-frame UV, and FIR continuum emission of Althæa at  $z = 6.0$  and Halo-12 at  $z = 6.5$  in the zoom-in simulations. The surface brightness morphology of the [C II] line emission clearly shows the extended structure over the 10 kpc scale with surrounding satellite clumps and filamentary structures. The picture of the extended [C II] halo around the central galaxies is roughly consistent with the observational results.

To quantitatively compare the zoom-in simulation to our observational results, we carry out the stacking for the zoom-in simulation results of the [C II] line, the rest-frame FIR, and the rest-frame UV continuum in the same manner as the observations. For the Althæa simulation, we take 12 snapshots at different redshifts within  $6.0 \leq z \leq 7.2$ . For each snapshot, we calculate the surface brightness from face-on and three random angles, where the [C II] line emissivity is calculated within  $100 \text{ km s}^{-1}$  of the velocity center of the galaxy to match the visibility-based stacking procedure for the ALMA data. In this way, we obtain 48 ( $12 \times 4$ ) images of Althæa. We refer to Kohandel et al. (2019) for a full analysis of the different morphological results from different evolutionary stages and viewing angles. We then select nine out of 48 snapshots randomly—the same sample size used for the stacking of the ALMA-*HST* sample. Finally, we perform the stacking of the intrinsic images and smooth the stacked images with the ALMA beam. For the second set of simulations, we calculate the surface brightness from three orthogonal angles for four different halos (Halo-12, Halo-A, Halo-B, Halo-C) and obtain 12 ( $4 \times 3$ ) images. We then carry out the same stacking and smoothing procedures as in the first simulation.

In the right panel of Figure 11, we show the radial surface brightness profiles estimated from the two independent zoom-in simulations. For comparison, we also plot the observational results obtained in Section 4. We find that both simulations reproduce the overall trend of observational results of the rest-frame UV and FIR continuum within the errors. However, we also find that the [C II] line emission in both simulations is not as extended as the observed data. In Althæa, although it reproduces the trend that the [C II] line is

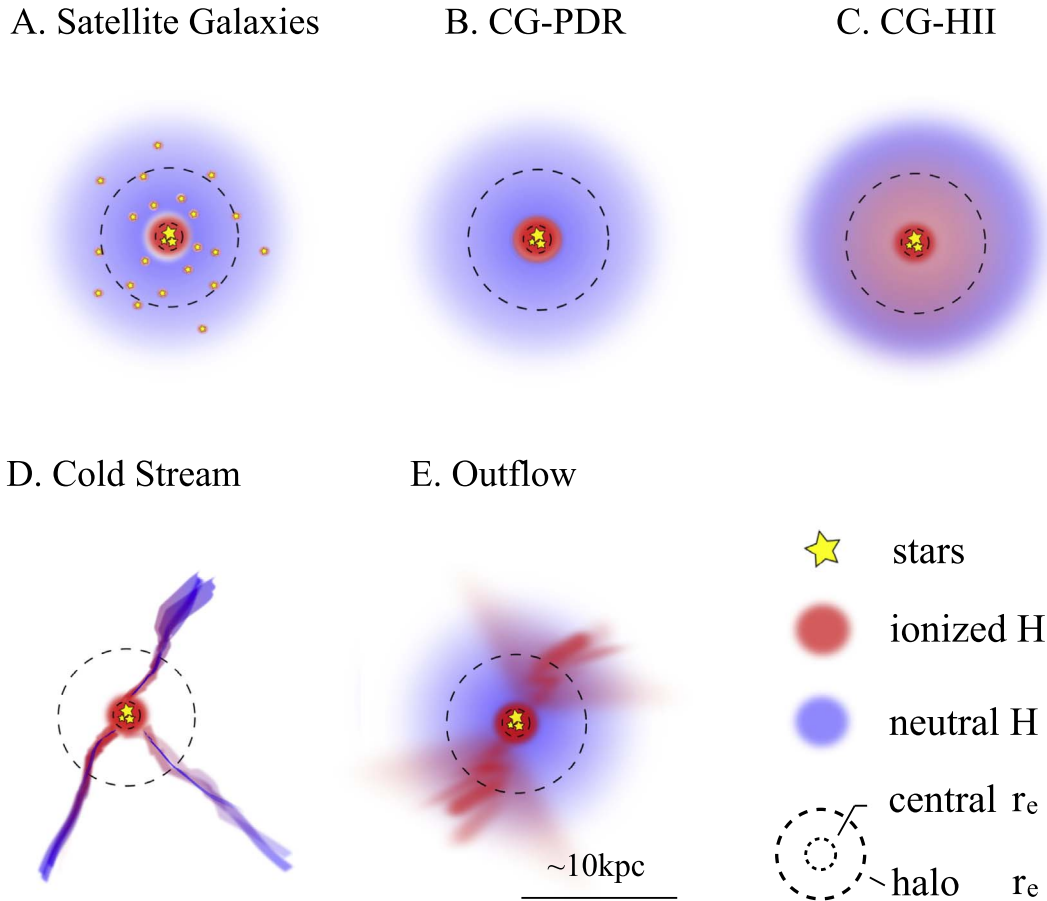


**Figure 12.** Illustrations of five possible scenarios for the physical origin of the [C II] halo with the potential association of the Ly $\alpha$  halo: (A) satellite galaxies, (B) CG PDR, (C) CG H II region (CG-H II), (D) cold stream, and (E) outflow. The blue and red shades show the neutral and ionized hydrogen in ISM and CGM. The yellow stars represent the star-forming regions. The inner and outer dashed circles denote the effective radii ( $r_e$ ) of the central and halo components of the [C II] line emission, respectively.

more extended than that of the rest-frame FIR and UV continuum, the intensity of the [C II] emission at  $r > 5$  kpc is still lower than the observed one. In Halo-12, the [C II] line is the least extended. These results indicate that the existence of the [C II] halo challenges current hydrodynamic simulations of galaxy formation.

## 5. Discussion

In Section 4, we find that the [C II] line emission is extended up to  $\sim 10$  kpc scale around the normal star-forming galaxies at  $z = 5-7$  and is potentially related to the Ly $\alpha$  halo. In contrast to the previous reports of the 10 kpc scale carbon reservoirs around rare, massive galaxies, such as dusty starbursts and quasars at  $z \sim 2-6$  (e.g., Ivison et al. 2011; Maiolino et al. 2012; Díaz-Santos et al. 2014; George et al. 2014; Ciccone et al. 2015; Falgarone et al. 2017), our results indicate that the cold carbon gas halo universally exists even around early normal galaxies.

The existence of cold carbon gas halos around early normal galaxies raises two questions: what powers the [C II] line emission, and how is the carbon abundance in the circumgalactic (CG) area enriched at such early cosmic epochs? Theoretical studies suggest the following five scenarios that can give rise to the extended [C II] line emission with the potential association of the Ly $\alpha$  halo:

- (A) satellite galaxies,
- (B) CG photodissociation region (PDR),
- (C) CG H II region,
- (D) cold streams,
- (E) outflow.

These five scenarios are illustrated in Figure 12.

The first scenario invokes satellite galaxies (Figure 12(A)). If satellite galaxies exist around the central star-forming galaxies, the [C II] and Ly $\alpha$  line emission from the satellite galaxies will be observed as extended structures around the central galaxies. In this scenario, the extended halo size is determined by the spatial distribution of the satellite galaxies, which explains both extended components of the [C II] and Ly $\alpha$  line emission.

The second scenario is a PDR extended over the CG scale, referred to as CG-PDR (Figure 12(B)). The ionizing photons ( $h\nu > 13.6$  eV) from massive stars form the H II region on the central galactic scale. Far-ultraviolet (FUV) photons ( $6 \text{ eV} < h\nu < 13.6 \text{ eV}$ ) penetrate the surrounding ISM deeper than the ionizing photons, making the PDR more extended than the H II region. In these PDRs, the carbon is still singly ionized (11.3 eV) by the FUV photons. If the PDR is extended over the CG scale, the extended [C II] line emission is thus detected on the CG scale. Besides, the Ly $\alpha$  line emission is also spatially extended by the resonant scattering by the neutral hydrogen in the surrounding ISM (e.g., Xue et al. 2017).



The third scenario is that ionizing photons penetrate the surrounding ISM deeper and form large H II regions, even spreading over the CGM, which we refer to as CG-H II (Figure 12(C)). This scenario is similar to scenario (B), but the existence of strong ionizing sources or ISM properties differs from scenario (B), and the H II region is larger than in scenario (B), where the carbon is singly ionized. In this case, the Ly $\alpha$  line emission is extended by the fluorescence (e.g., Mas-Ribas & Dijkstra 2016), instead of the resonance scattering in scenario (B).

The fourth scenario is cold streams (Figure 12(D)). Cosmological hydrodynamical simulations suggest that intense star formation in high- $z$  galaxies is fed by a dense and cold gas ( $\sim 10^4$  K), which is dubbed cold streams (e.g., Dekel et al. 2009). The cold streams radiate [C II] as well as Ly $\alpha$  line emission powered by gravitational energy and produce the extended [C II] and Ly $\alpha$  line emission around a galaxy. Moreover, the cold stream may cause shock heating, which can also produce the [C II] and Ly $\alpha$  line emission.

The fifth scenario is outflow (Figure 12(E)). In the outflow, the ionized carbon and hydrogen powered by the AGN or star formation feedback produce the extended [C II] and Ly $\alpha$  line emission (see also Faisst et al. 2017). The associated process of shock heating may also contribute to radiating these line emissions. Note that although we choose ALMA sources not reported as AGNs, we cannot rule out the possibility that our ALMA sources contain faint AGNs or have past AGN activity.

In the following subsections, we discuss these possibilities based on the observational and theoretical results.

### 5.1. Hints from Observational Results

In the observational results, the [C II] line is more extended than both the rest-frame FIR dust and UV continuum beyond the errors up to a radius of at least  $\sim 7$  kpc (Figure 6). Assuming a constant [C II] line emissivity at a given stellar continuum (De Looze et al. 2014), the large gap between the radial profiles of the [C II] line and the stellar continuum indicates that the stellar continuum is not enough to explain the large part of the [C II] line emissivity of the [C II] halo.

Although the [C II] line emissivity may be changed from the central to the halo areas at a given stellar continuum, the metallicity at such outer areas is expected to be  $\sim 1\%$  of the galaxy center (Pallottini et al. 2017a). Even if the stellar continuum in the outskirts is coming from low-mass, faint satellite galaxies, the mass–metallicity relation (Mannucci et al. 2010) also suggests lower metallicities for the satellite galaxies. Because lower metallicity reduces the [C II] line emissivity for a given stellar continuum (Vallini et al. 2015), it would be difficult to explain the [C II] halo by the same source as the stellar continuum. In fact, Figure 8 shows that the  $L_{[\text{C II}]} / \text{SFR}_{\text{total}}$  ratio becomes higher toward the outskirts of the halo, which cannot be explained by the dwarf galaxies. Our observational results thus rule out scenario (A) and support the other four scenarios.

In the recent [C II] line studies at  $z > 5$ , Gallerani et al. (2018) report signatures of starburst-driven outflows from nine normal star-forming galaxies at  $z \sim 5.5$  with the stacked [C II] spectra. With a similar sample, the rest-frame UV metal absorptions are also identified to be blueshifted from the [C II] systemic redshift in the stacked Keck spectra (Sugahara et al. 2019). From more luminous objects, broad wing features are detected in the stacked [C II] line spectra of  $z \sim 4\text{--}6$  quasars (Bischetti et al. 2019), as well as in an individual [C II] line spectrum of a quasar at  $z = 6.4$  (Maiolino et al. 2012; Ciccone

et al. 2015). These recent results suggest that scenario (E) may be potentially very interesting. However, it is also reported that the stacked [C II] spectra even from 23 quasars at  $z \gtrsim 6$  show no clear evidence for the existence of strong feedback (Decarli et al. 2018). Also, our stacked [C II] spectra with the 18 star-forming galaxies do not show a clear, broad wing feature either (Section 4.5). Among scenarios (B), (C), (D), and (E), we thus cannot choose the most likely one from our and other recent observational results.

### 5.2. Hints from Theoretical Results

In the simulation results, the extended profile of the [C II] halo is not fully reproduced (Figure 11). This may suggest that some physical processes are not sufficiently solved in the simulations, such as metal enrichment, feedback, ISM/CGM clumpiness, and the propagation of ionizing radiation. On the other hand, if the current assumptions related to the [C II] line emissivity are correct, additional mechanism(s) are required to produce the extended [C II] line emissivity in the simulation.

There are two possibilities for such additional mechanisms that are not included in the calculation of [C II] line emissivity in the simulations. The first possible mechanism is shock heating; Appleton et al. (2013) have shown that [C II] can be excited on large scales from the dissipation of mechanical energy of galaxy mergers via a turbulent cascade. Although the shock heating should be captured in the hydrodynamical calculation of the zoom-in simulation, it is possible that the current simulations do not have sufficient resolution to capture the turbulent cascade of large-scale mechanical energy down to the molecular cloud scales. This means that the computation of the ionized carbon abundance in CLOUDY does not adequately consider the effect of shock heating. Since shock heating is caused by galaxy merger or gas inflow/outflow processes, the [C II] emissivity could become more enhanced if the shock heating and associated turbulent cascade are properly treated in scenarios (A), (D), and (E).

The second possible mechanism is the past or ongoing AGN activities, which could form a large H II region and surrounding PDR. Moreover, the AGN feedback may cause shock heating, which also could contribute to the [C II] line emissivity. In this case, scenarios (C) and (E) are further supported.

Note that if the effect of shocks and AGNs is too strong, the carbon may be doubly ionized, and then the [C II] line is rarely emitted. Therefore, it is hard to conclude whether the missing treatments of shocks or AGNs in the current simulations are the major causes of the inadequate [C II] halo in the simulations.

It should also be noted that seven out of nine sources in the ALMA-*HST* sample are placed at  $5 < z < 6$ , when the effect of the CMB is weaker than at  $z = 6.0\text{--}7.2$ , from which the zoom-in simulation results were taken. Because the CMB effect reduces the line luminosity from the diffuse component (e.g., da Cunha et al. 2013; Pallottini et al. 2015; Zhang et al. 2016; Lagache et al. 2018), the slight difference in the redshift range may cause the insufficient [C II] line luminosity in the zoom-in simulation results.

### 5.3. Physical Origin of [C II] Halo

We summarize the possible scenarios for what powers the [C II] halo based on the results of Sections 5.1–5.2. From the observational results, we rule out scenario (A). In the zoom-in simulation results, it is hard to conclude which scenario is the most plausible one unless we perform further analyses with

different models of supernova (SN) and AGN feedback, for example. The possible scenarios at this point are thus (B), (C), (D), and (E) given the current best estimates of both observational and theoretical results.

Most importantly, the outflow activities are required in all cases to enrich the CGM with carbon around the normal star-forming galaxies in the early universe. Our results are thus evidence of outflow remnants in these early star-forming galaxies.

There are two modes of outflows: hot-mode and cold-mode outflows (e.g., Murray et al. 2011; Hopkins et al. 2014; Muratov et al. 2015; Heckman & Thompson 2017). The hot-mode outflow is defined as the outflow of ionized hydrogen (hot) gas that is heated by SN explosions and massive star/AGN radiation. Since the cooling time of such hot gas ( $\gtrsim 10^6$  K) can be longer than the cosmic time at  $z \sim 5-7$  ( $\sim 1$  Gyr; e.g., Madau et al. 2001), it would be difficult to produce the [C II]-emitting cold halos from the hot-mode outflow. On the other hand, the cold-mode outflow consists of the cold neutral hydrogen gas that is pushed by the radiative and kinetic pressures exerted by SNe, massive stars, and AGNs. In this case, the majority of [C II] line emission would be radiated from the PDR in the cold, neutral hydrogen gas clouds. Therefore our finding of the [C II] halo suggests that outflows in the early star-forming galaxies may be dominated by the cold-mode outflows.

Since we also find similarity in the radial surface brightness profiles between the [C II] and  $\text{Ly}\alpha$  halos (Figure 9), the physical origin of the [C II] halo may be related to the  $\text{Ly}\alpha$  halo. Future deep observations of both [C II] and  $\text{Ly}\alpha$  line emission for individual high- $z$  galaxies are required to comprehensively understand the mechanism of the CGM metal enrichment with the theoretical simulations, including the radiative transfers of these line emissions.

## 6. Summary

In this paper, we study the detailed morphology of [C II] line emission via the ALMA visibility-based stacking method for normal star-forming galaxies whose [C II] line has been individually detected at  $z = 5.153-7.142$ . The visibility-based stacking achieves deep and well-sampled visibility data in the  $uv$ -plane, which enables us to securely investigate the diffuse emission extended over the circumgalactic environment. In conjunction with the deep *HST*/*H*-band data, we examine the radial surface brightness profiles of the [C II] line, rest-frame FIR, and UV continuum emission. We then discuss the physical origin of the extended [C II] line emission. The major findings of this paper are summarized below.

1. The visibility-based stacking of our and archival deep ALMA data for 18 galaxies with  $\text{SFR} \simeq 10-70 M_{\odot} \text{ yr}^{-1}$  at  $z = 5.153-7.142$  produces  $21\sigma$  and  $10\sigma$  level detections at the peak for the [C II] line and dust continuum emission, respectively. The stacked [C II] line morphology is spatially extended more than that of the dust continuum. The radial surface brightness profiles of the [C II] line are extended up to a radius of  $\sim 10$  kpc at the  $9.2\sigma$  level.
2. The *HST*/*H*-band stacking for nine out of the 18 [C II] line sources that are taken by the deep *HST* observations shows that the radial surface brightness profiles of the [C II] line are significantly extended more than that of the rest-frame UV or the rest-frame FIR continuum emission. We derive the radial ratio of  $L_{[\text{C II}]} / \text{SFR}_{\text{total}}$ , showing that the ratio becomes higher toward the outskirts of the halo,

where the high ratios cannot be explained by satellite galaxies.

3. The two-component Sérsic+exponential profile fitting results indicate that the extended [C II] halo component has a scale length of  $3.3 \pm 0.1$  kpc, which is comparable to the  $\text{Ly}\alpha$  halo, universally found around the high- $z$  star-forming galaxies. In terms of effective radius, the extended [C II] halo component is larger than the central galactic component by a factor of  $\sim 5$ .
4. The state-of-the-art zoom-in cosmological hydrodynamic simulations roughly reproduce the radial surface brightness profile trends of the extended [C II] line emission and the rest-frame FIR, comparable to the rest-frame UV continuum emission. However, the simulations do not reproduce the full extent of the [C II] halo in the outskirts, where the simulations might be missing some physical mechanisms associated with the feedback, or still lacking the resolution to resolve the turbulent cascade from large-scale shocks down to the small scales of molecular clouds, if such a process is indeed important for the [C II] emission in high- $z$  galaxies, as Appleton et al. (2013) argued.
5. Although several possible scenarios remain that can give rise to [C II] line emission in the CGM, the outflow is required in any cases to enrich the primordial CGM with carbon around the early star-forming galaxies. Our results are thus evidence of outflow remnants in the early star-forming galaxies and suggest that the outflow may be dominated by the cold-mode outflow.

We are grateful to Ivan Marti-Vidal and the Nordic ALMA Regional Center for providing us with helpful CASA software tools and advice on analyzing the data. We appreciate Tohru Nagao, Jeremy Blaizot, Peter Mitchell, Takashi Kojima, Shiro Mukae, Yuichi Harikane, Akio Inoue, and Rieko Momose for useful comments and suggestions. We are indebted for the support of the staff at the ALMA Regional Center. This paper makes use of the following ALMA data: ADS/JAO, ALMA #2013.1.00815.S, #2015.1.00834.S, #2015.1.01111.S, #2015.1.01105, #2016.1.01240.S, #2012.1.00523.S, and #2012.1.00602.S. ALMA is a partnership of the ESO (representing its member states), NSF (USA), and NINS (Japan), together with NRC (Canada), *MOST* and ASIAA (Taiwan), and KASI (Republic of Korea), in cooperation with the Republic of Chile. The Joint ALMA Observatory is operated by the ESO, AUI/NRAO, and NAOJ. This study is supported by World Premier International Research Center Initiative (WPI Initiative), MEXT, Japan, and KAKENHI (15H02064, 16J02344, 17H01110, 17H01111, and 17H01114) Grant-in-Aid for Scientific Research (A) through the Japan Society for the Promotion of Science (JSPS), the Grant-in-Aid for JSPS Research Fellow, the NAOJ ALMA Scientific Research grant No. 2017-06B, and the Munich Institute for Astro- and Particle Physics (MIAPP) of the DFG cluster of excellence “Origin and Structure of the Universe.” S.F. is supported by the ALMA Japan Research Grant of NAOJ Chile Observatory NAOJ-ALMA-197, The 2018 Graduate Research Abroad in Science Program Grant (GRASP2018), and the Hayakawa Satio Fund awarded by the Astronomical Society of Japan. A.F. and R.J.I. acknowledge support from the ERC Advanced Grant INTERSTELLAR H2020/740120 and COSMIC ISM 321302, respectively.

### Appendix Our ALMA Sample

The sources drawn from the literature in our ALMA sample are summarized in Table 1. For this literature sample, Figure 13 shows the [C II] line velocity-integrated maps and the spectra

obtained from our reanalysis of the archival ALMA data. We confirm that the spatial morphology and the spectrum shape of the [C II] lines are consistent with previous studies (Capak et al. 2015; Willott et al. 2015; Pentericci et al. 2016; Carniani et al. 2018; Smit et al. 2018).

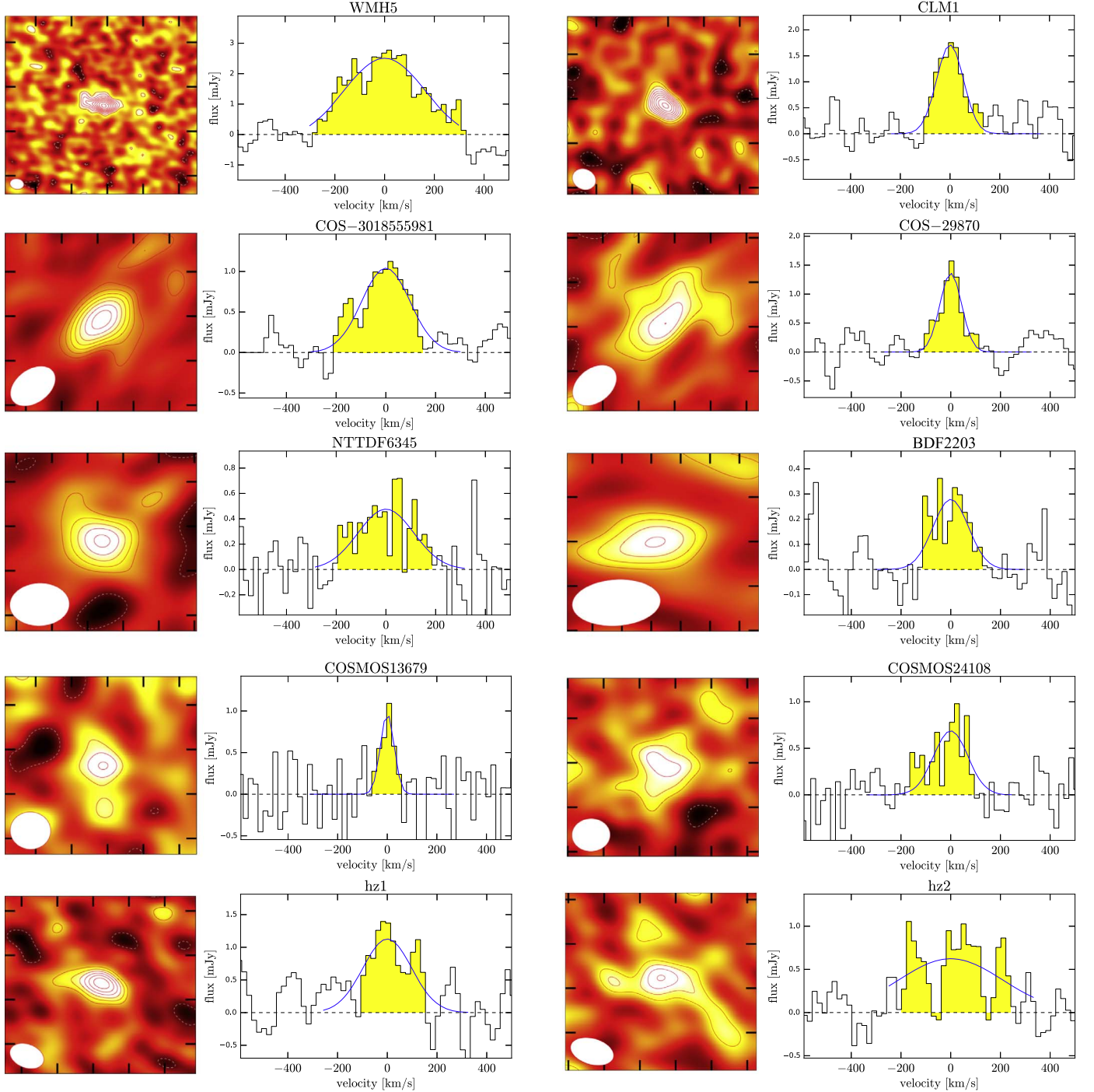


**Figure 13.** [C II] line velocity-integrated map (left) and spectrum (right) obtained in our reanalysis of the archival ALMA data for the literature sample in Table 1. Left: natural-weighted  $4'' \times 4''$  field image of the velocity-integrated [C II] line intensity (moment zero) with contours at the  $-2\sigma$  (white),  $2\sigma$ ,  $3\sigma$ , ...,  $10\sigma$  (red) levels. The synthesized beam is presented at the bottom left. North is up, and east is to the left. Right: [C II] line spectrum with an aperture diameter of  $1''/2$ . The blue curve denotes the best-fit profile of the single Gaussian. Here, we perform the fitting in the velocity range  $\pm 300 \text{ km s}^{-1}$  from the [C II] line frequency center estimated in the previous studies. The yellow shades present the integrated velocity range for the [C II] line intensity map presented in the left panel. The velocities are relative to the center of the best-fit Gaussian.



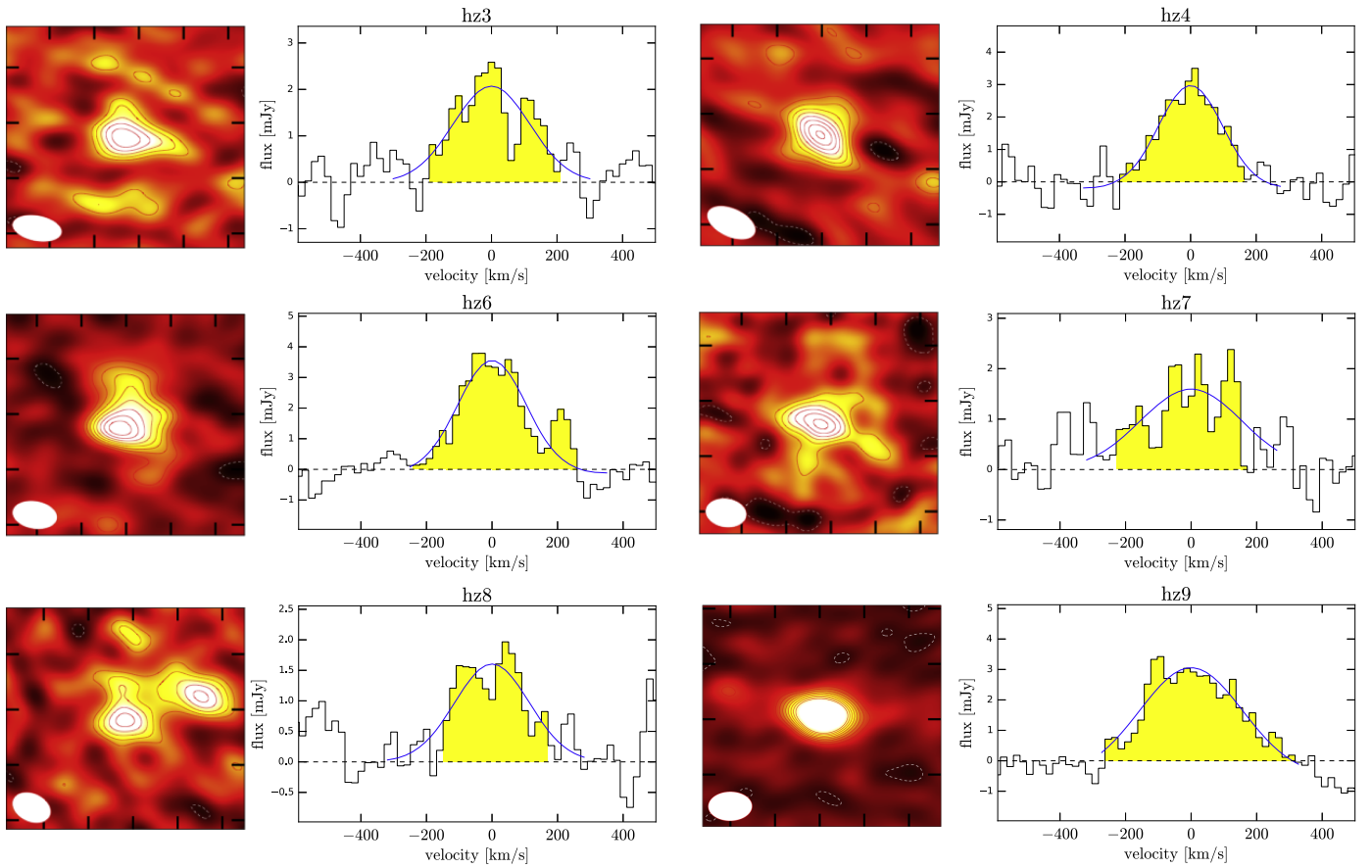


Figure 13. (Continued.)

## ORCID iDs

Seiji Fujimoto <https://orcid.org/0000-0001-7201-5066>  
 Masami Ouchi <https://orcid.org/0000-0002-1049-6658>  
 Andrea Ferrara <https://orcid.org/0000-0002-9400-7312>  
 R. J. Ivison <https://orcid.org/0000-0001-5118-1313>  
 Kentaro Nagamine <https://orcid.org/0000-0001-7457-8487>

## References

- Appleton, P. N., Guillard, P., Boulanger, F., et al. 2013, *ApJ*, **777**, 66  
 Arata, S., Yajima, H., Nagamine, K., Li, Y., & Khochfar, S. 2019a, *arXiv:1908.01438*  
 Arata, S., Yajima, H., Nagamine, K., Li, Y., & Khochfar, S. 2019b, *MNRAS*, **488**, 2629  
 Aravena, M., Decarli, R., Walter, F., et al. 2016, *ApJ*, **833**, 71  
 Barisic, I., Faisst, A. L., Capak, P. L., et al. 2017, *ApJ*, **845**, 41  
 Behrens, C., Pallottini, A., Ferrara, A., Gallerani, S., & Vallini, L. 2018, *MNRAS*, **477**, 552  
 Bertin, E., & Arnouts, S. 1996, *A&A*, **117**, 393  
 Bischetti, M., Maiolino, R., Fiore, S. C. F., Piconcelli, E., & Fluetsch, A. 2019, *A&A*, **630**, A59  
 Bouwens, R. J., van Dokkum, P. G., Illingworth, G. D., et al. 2017, *arXiv:1711.02090*  
 Capak, P. L., Carilli, C., Jones, G., et al. 2015, *Natur*, **522**, 455  
 Carniani, S., Maiolino, R., Amorin, R., et al. 2018, *MNRAS*, **478**, 1170  
 Ciccone, C., Maiolino, R., Gallerani, S., et al. 2015, *A&A*, **574**, A14  
 Coppin, K., Halpern, M., Scott, D., et al. 2008, *MNRAS*, **384**, 1597  
 Cullen, F., McLure, R. J., Khochfar, S., Dunlop, J. S., & Dalla Vecchia, C. 2017, *MNRAS*, **470**, 3006  
 da Cunha, E., Groves, B., Walter, F., et al. 2013, *ApJ*, **766**, 13  
 Decarli, R., Walter, F., Venemans, B. P., et al. 2018, *ApJ*, **854**, 97  
 Dekel, A., Birnboim, Y., Engel, G., et al. 2009, *Natur*, **457**, 451  
 De Looze, I., Cormier, D., Leboutteiller, V., et al. 2014, *A&A*, **568**, A62  
 Díaz-Santos, T., Armus, L., Charmandaris, V., et al. 2014, *ApJL*, **788**, L17  
 Dunlop, J. S., McLure, R. J., Biggs, A. D., et al. 2017, *MNRAS*, **466**, 861  
 Faisst, A. L., Capak, P. L., Yan, L., et al. 2017, *ApJ*, **847**, 21  
 Falgarone, E., Zwaan, M. A., Godard, B., et al. 2017, *Natur*, **548**, 430  
 Ferland, G. J., Chatzikos, M., Guzmán, F., et al. 2017, *RMxAA*, **53**, 385  
 Fujimoto, S., Ouchi, M., Kohno, K., et al. 2018, *ApJ*, **861**, 7  
 Fujimoto, S., Ouchi, M., Ono, Y., et al. 2016, *ApJS*, **222**, 1  
 Fujimoto, S., Ouchi, M., Shibuya, T., & Nagai, H. 2017, *ApJ*, **850**, 1  
 Gaia Collaboration, Brown, A. G. A., Vallenari, A., et al. 2018, *A&A*, **616**, A1  
 Gallerani, S., Pallottini, A., Feruglio, C., et al. 2018, *MNRAS*, **473**, 1909  
 George, R. D., Ivison, R. J., Smail, I., et al. 2014, *MNRAS*, **442**, 1877  
 Harikane, Y., Ouchi, M., Ono, Y., et al. 2018, *PASJ*, **70**, S11  
 Hashimoto, T., Inoue, A. K., Mawatari, K., et al. 2019, *PASJ*, **71**, 71  
 Hayatsu, N. H., Matsuda, Y., Umehata, H., et al. 2017, *PASJ*, **69**, 45  
 Heckman, T. M., & Thompson, T. A. 2017, in *Handbook of Supernovae*, ed. A. W. Alsabti & P. Murdin (Cham: Springer), 2431  
 Hodge, J. A., Swinbank, A. M., Simpson, J. M., et al. 2016, *ApJ*, **833**, 103  
 Hopkins, P. F., Kereš, D., Oñorbe, J., et al. 2014, *MNRAS*, **445**, 581  
 Ikarashi, S., Ivison, R. J., Caputi, K. I., et al. 2015, *ApJ*, **810**, 133  
 Ilbert, O., McCracken, H. J., Le Fèvre, O., et al. 2013, *A&A*, **556**, A55  
 Ivison, R. J., Papadopoulos, P. P., Smail, I., et al. 2011, *MNRAS*, **412**, 1913  
 Johnson, J. L., Dalla Vecchia, C., & Khochfar, S. 2013, *MNRAS*, **428**, 1857  
 Jones, G. C., Willott, C. J., Carilli, C. L., et al. 2017, *ApJ*, **845**, 175  
 Kawamata, R., Ishigaki, M., Shimasaku, K., et al. 2018, *ApJ*, **855**, 4  
 Knudsen, K. K., Richard, J., Kneib, J.-P., et al. 2016, *MNRAS*, **462**, L6  
 Kohandel, M., Pallottini, A., Ferrara, A., et al. 2019, *MNRAS*, **487**, 3007  
 Lagache, G., Cousin, M., & Chatzikos, M. 2018, *A&A*, **609**, A130  
 Leclercq, F., Bacon, R., Wisotzki, L., et al. 2017, *A&A*, **608**, A8  
 Li, Y., Hopkins, P. F., Hernquist, L., et al. 2008, *ApJ*, **678**, 41  
 Lindroos, L., Knudsen, K. K., Vlemmings, W., Conway, J., & Martí-Vidal, I. 2015, *MNRAS*, **446**, 3502  
 Madau, P., Ferrara, A., & Rees, M. J. 2001, *ApJ*, **555**, 92  
 Maiolino, R., Carniani, S., Fontana, A., et al. 2015, *MNRAS*, **452**, 54  
 Maiolino, R., Gallerani, S., Neri, R., et al. 2012, *MNRAS*, **425**, L66  
 Mannucci, F., Cresci, G., Maiolino, R., Marconi, A., & Gnerucci, A. 2010, *MNRAS*, **408**, 2115



- Martí-Vidal, I., Vlemmings, W. H. T., Muller, S., & Casey, S. 2014, *A&A*, **563**, A136
- Mas-Ribas, L., & Dijkstra, M. 2016, *ApJ*, **822**, 84
- Matsuda, Y., Yamada, T., Hayashino, T., et al. 2012, *MNRAS*, **425**, 878
- Matthee, J., Sobral, D., Boone, F., et al. 2017, *ApJ*, **851**, 145
- Matthee, J., Sobral, D., Santos, S., et al. 2015, *MNRAS*, **451**, 400
- McMullin, J. P., Waters, B., Schiebel, D., Young, W., & Golap, K. 2007, in ASP Conf. Ser. 376, *Astronomical Data Analysis Software and Systems XVI*, ed. R. A. Shaw, F. Hill, & D. J. Bell (San Francisco, CA: ASP), 127
- Momose, R., Ouchi, M., Nakajima, K., et al. 2014, *MNRAS*, **442**, 110
- Momose, R., Ouchi, M., Nakajima, K., et al. 2016, *MNRAS*, **457**, 2318
- Muratov, A. L., Kereš, D., Faucher-Giguère, C.-A., et al. 2015, *MNRAS*, **454**, 2691
- Murphy, E. J., Condon, J. J., Schinnerer, E., et al. 2011, *ApJ*, **737**, 67
- Murray, N., Ménard, B., & Thompson, T. A. 2011, *ApJ*, **735**, 66
- Oesch, P. A., Bouwens, R. J., Carollo, C. M., et al. 2010, *ApJL*, **725**, L150
- Oke, J. B., & Gunn, J. E. 1983, *ApJ*, **266**, 713
- Ono, Y., Ouchi, M., Curtis-Lake, E., et al. 2013, *ApJ*, **777**, 155
- Ouchi, M., Mobasher, B., Shimasaku, K., et al. 2009, *ApJ*, **706**, 1136
- Ouchi, M., Shimasaku, K., Akiyama, M., et al. 2008, *ApJS*, **176**, 301
- Ouchi, M., Shimasaku, K., Furusawa, H., et al. 2010, *ApJ*, **723**, 869
- Pallottini, A., Ferrara, A., Bovino, S., et al. 2017a, *MNRAS*, **471**, 4128
- Pallottini, A., Ferrara, A., Gallerani, S., et al. 2017b, *MNRAS*, **465**, 2540
- Pallottini, A., Gallerani, S., Ferrara, A., et al. 2015, *MNRAS*, **453**, 1898
- Peng, C. Y., Ho, L. C., Impey, C. D., & Rix, H.-W. 2010, *AJ*, **139**, 2097
- Pentericci, L., Carniani, S., Castellano, M., et al. 2016, *ApJL*, **829**, L11
- Planck Collaboration, Abergel, A., Ade, P. A. R., et al. 2011, *A&A*, **536**, A21
- Rujopakarn, W., Dunlop, J. S., Rieke, G. H., et al. 2016, *ApJ*, **833**, 12
- Rybak, M., Calistro Rivera, G., Hodge, J. A., et al. 2019, *ApJ*, **876**, 112
- Schaye, J., Dalla Vecchia, C., Booth, C. M., et al. 2010, *MNRAS*, **402**, 1536
- Sérsic, J. L. 1963, *BAAA*, **6**, 41
- Shibuya, T., Ouchi, M., & Harikane, Y. 2015, *ApJS*, **219**, 15
- Simpson, J. M., Smail, I., Swinbank, A. M., et al. 2015, *ApJ*, **799**, 81
- Skelton, R. E., Whitaker, K. E., Momcheva, I. G., et al. 2014, *ApJS*, **214**, 24
- Smit, R., Bouwens, R. J., Carniani, S., et al. 2018, *Natur*, **553**, 178
- Smit, R., Bouwens, R. J., Franx, M., et al. 2015, *ApJ*, **801**, 122
- Springel, V. 2005, *MNRAS*, **364**, 1105
- Stacey, G. J., Geis, N., Genzel, R., et al. 1991, *ApJ*, **373**, 423
- Steidel, C. C., Bogosavljević, M., Shapley, A. E., et al. 2011, *ApJ*, **736**, 160
- Sugahara, Y., Ouchi, M., Harikane, Y., et al. 2019, *ApJ*, in press (arXiv:1904.03106)
- Vallini, L., Gallerani, S., Ferrara, A., Pallottini, A., & Yue, B. 2015, *ApJ*, **813**, 36
- Venemans, B. P., Neeleman, M., Walter, F., et al. 2019, *ApJL*, **874**, L30
- Watson, D., Christensen, L., Kraiberg Knudsen, K., et al. 2015, *Natur*, **519**, 327
- Willott, C. J., Carilli, C. L., Wagg, J., & Wang, R. 2015, *ApJ*, **807**, 180
- Willott, C. J., McLure, R. J., Hibon, P., et al. 2013a, *AJ*, **145**, 4
- Willott, C. J., Omont, A., & Bergeron, J. 2013b, *ApJ*, **770**, 13
- Xue, R., Lee, K.-S., Dey, A., et al. 2017, *ApJ*, **837**, 172
- Yajima, H., Li, Y., Zhu, Q., & Abel, T. 2012, *MNRAS*, **424**, 884
- Yajima, H., Nagamine, K., Zhu, Q., Khochfar, S., & Dalla Vecchia, C. 2017, *ApJ*, **846**, 30
- Zhang, Z.-Y., Papadopoulos, P. P., Ivison, R. J., et al. 2016, *RSOS*, **3**, 160025